

1

## 2 **Multi-Physics Analyses of Selected Civil** 3 **Engineering Concrete Structures**

4 J. Kruis\*, T. Koudelka and T. Krejčí

5 *Department of Mechanics, Faculty of Civil Engineering, Czech Technical University,*  
6 *Thákurova 7, Prague, 166 29, Czech Republic.*

8 Received XXX; Accepted (in revised version) XXX

9 Available online xxx

10

---

**Abstract.** This paper summarizes suitable material models for creep and damage of concrete which are coupled with heat and moisture transfer. The fully coupled approach or the staggered coupling is assumed. Governing equations are spatially discretized by the finite element method and the temporal discretization is done by the generalized trapezoidal method. Systems of non-linear algebraic equations are solved by the Newton method. Development of an efficient and extensible computer code based on the C++ programming language is described. Finally, successful analyses of two real engineering problems are described.

11 **AMS subject classifications:** 74C10, 74F05, 74F10, 74R05, 74S05, 76R50, 80A20, 80M10

12 **Key words:** Coupled problems, heat and moisture transfer, creep, damage mechanics, hydro-  
13 thermo-mechanical analysis, efficient solvers, analysis of containment, watertightness of founda-  
14 tion slabs.

15

---

## 16 **1 Introduction**

17 Analyses of many engineering and scientific problems become more complicated in the  
18 course of time because the multiphysics approach is required in branches where the sin-  
19 gle physics was satisfactory several years ago. Civil engineering is not an exception  
20 which can be documented on coupled analyses used for very important and monumen-  
21 tal structures. Usually the mechanical analysis coupled with heat and moisture transfer  
22 is considered. The multiphysics approach can be used because of large achievements  
23 in numerical methods and significant development of computers, especially the parallel  
24 computers.

---

\*Corresponding author. *Email addresses:* jk@cml.fsv.cvut.cz (J. Kruis), koudelka@cml.fsv.cvut.cz (T. Koudelka), krejci@cml.fsv.cvut.cz (T. Krejčí)

25 From many multiphysics problems of civil engineering, this paper concentrates only  
26 on the coupled hydro-thermo-mechanical analysis of concrete structures. The paper de-  
27 scribes selected material models for mechanical and transport processes, balance and  
28 governing equations, their approximation by the finite element method, efficient meth-  
29 ods for time discretization and solvers of algebraic equations. Special attention is devoted  
30 to development of a computer code which has to be easily extensible and very efficient.  
31 At the end, some real world engineering problems solved by the authors during past five  
32 years are described.

33 Concrete represents a very specific material which requires multiphysics analysis be-  
34 cause the mechanical behaviour depends strongly on distribution of moisture and tem-  
35 perature. In the past, moisture and temperature were assumed time independent or they  
36 were not taken into account at all. The coupled hydro-thermo-mechanical approach en-  
37 ables description of real conditions and the material and structural response is in accor-  
38 dance with experiments.

39 The classical mechanical analysis based on the finite element method defines two or  
40 three unknown displacements in nodes of the mesh with respect to the dimension of  
41 problem solved. Heat and moisture transfer can be described by models which define  
42 two or three unknown nodal values. The unknowns represent nodal temperature, mois-  
43 ture content, relative humidity or partial pressures. In the general three-dimensional  
44 case, the coupled analysis deals with six unknowns in each node of the mesh. It is clear  
45 that the requirements on computers grow rapidly with the growing number of nodes in  
46 the mesh.

47 The classical single processor implementation of coupled problems gives severe lim-  
48 its on finite element mesh. Unfortunately, the mesh has to take into account the shape  
49 of the structure solved as well as possible steep gradients of all unknown variables.  
50 Only two-dimensional or very simple three-dimensional problems can be treated on a  
51 single processor computer. On the other hand, parallel computers with several proces-  
52 sors together with domain decomposition methods represent a very efficient tool which is  
53 able to deal with significantly larger problems and reasonably fine meshes. The domain  
54 decomposition methods were successfully applied in various problems in past twenty  
55 years [9, 19–21, 31, 34, 40].

56 Another possibility of efficient solution of complicated multiphysics problems is ap-  
57 plication of adaptive methods. It is known, that there are basically three types of adaptive  
58 methods connected with the finite element approach. The h-version changes the meshes  
59 while the degree of polynomials used for approximation on finite elements is constant.  
60 On the other hand, the p-version changes the degree of polynomials used while the finite  
61 element mesh is fixed. Finally, the most efficient hp-version combines the previous ap-  
62 proaches, i.e. the mesh and the degree of polynomials are changed simultaneously [36].  
63 Clearly, the hp-version is the most difficult version in the perspective of computer imple-  
64 mentation but it saves significant number of degrees of freedom which leads to shorter  
65 computational time and smaller demands on computer memory [37].

66 The paper is organized as follows. Section 2 summarizes useful mechanical material

67 models for concrete which are applied in pure mechanical analyses and coupled analyses  
68 as well. Models of creep, isotropic and orthotropic damage are mentioned. Section 3 is  
69 devoted to models of heat and moisture transfer. Namely, Künzel and Kiessl's model is  
70 described. Section 4 deals with numerical methods for time discretization and the New-  
71 ton method for solution of non-linear algebraic equations. Section 5 describes implemen-  
72 tation of material models, numerical methods and solvers. Requirements on extensibility  
73 and performance efficiency are also taken into account. The last section 6 describes se-  
74 lected real engineering problems solved. The analysis of watertightness of a foundation  
75 slab and simulation of a reactor vessel are mentioned in detail.

## 76 2 Mechanical models

Concrete is heterogeneous material whose behaviour is very complex. Creep, shrinkage, thermal dilatancy, plasticity, damage and crack propagation are the most important phenomena which should be taken into account for concrete modelling. Usually, the models describe only one aspect of concrete behaviour and this leads to combination of several material models. Assuming small strains, the total strain can be additively decomposed into several parts

$$\varepsilon = \varepsilon_e + \varepsilon_p + \varepsilon_d + \varepsilon_c + \varepsilon_{sh} + \varepsilon_t, \quad (2.1)$$

where  $\varepsilon$  denotes the total strain,  $\varepsilon_e$  denotes the elastic strain,  $\varepsilon_p$  stands for the plastic strain,  $\varepsilon_d$  stands for damage strain,  $\varepsilon_c$  is creep strain which contains also contributions caused by ageing,  $\varepsilon_{sh}$  denotes part of strain caused by shrinkage and  $\varepsilon_t$  is free thermal strain. The resulting stress  $\sigma$  can be expressed from the Hook's law of elasticity in the form

$$\sigma = D_e \varepsilon_e, \quad (2.2)$$

77 where  $D_e$  is the elastic stiffness of material.

78 Following subsections summarize models based on small strains used for analyses of  
79 real concrete structures described in this paper. In the case of geometrical non-linearity,  
80 the additive strain decomposition is not acceptable and different approach has to be used  
81 (e.g. [26]). The models described can be applied to matured concrete while special models  
82 have to be used for very early ages [38].

### 83 2.1 Concrete creep, effect of moisture and temperature

84 When taking into account the effects included in equation (2.1), the creep strain is most  
85 influenced by the moisture and temperature distribution and their history. Therefore,  
86 the creep has to be coupled with the heat and moisture transfer in order to obtain close  
87 agreement between numerical simulation and experiments. There are special problems,  
88 e.g. analysis of containment and reactor vessels in nuclear power plants, watertightness  
89 of foundation slabs or long term behaviour of long-span bridges, where the creep of  
90 concrete plays a very important role.

The areas of application of coupled heat and moisture transfer models are much more extensive. They also include problems such as energy storage and recovery, geothermal storage, nuclear waste disposal, evaluating the safety of peculiar concrete structures, and many others. The magnitude of pore pressures and the loss of moisture caused by heating of concrete is of considerable concern for predicting the response of prestressed concrete reactor vessels to hypothetical core disruption accidents as well as the response of concrete structures to fire. When solving the latter problem, a suitable constitutive law is required to describe the time-dependent behaviour of a structure due to shrinkage and creep. Pore relative humidity and temperature influence the creep and shrinkage in two ways – directly, by varying the viscosity coefficients in a constitutive model, and indirectly, through the effect of the rate of hydration (ageing). Temperature and pore humidity have also the direct effect on the rate of creep. To this end, the most convenient representations of compliance  $J(t, t')$  in terms of the Dirichlet-Prony series are considered

$$J(t, t') = \sum_{\mu=1}^M \frac{1}{D_{\mu}(t')} \{1 - \exp [y_{\mu}(t') - y_{\mu}(t)]\}, \quad (2.3)$$

91 where  $y(t)_{\mu} = (t/\tau_{\mu})^{q_{\mu}}$ ,  $q_{\mu} \leq 1$  is a coefficient (usually  $q_{\mu} = \frac{2}{3}$ ). The compliance function  
 92 of a linear viscoelastic material represents the strain at time  $t$  due to a unit stress  $\sigma = 1$   
 93 applied at time  $t'$ . A proper selection of retardation times  $\tau_{\mu}$  for  $J(t, t')$  can be found  
 94 in [2]. Functions  $D_{\mu}$  are usually obtained by fitting the compliance functions (2.3) using  
 95 the method of least squares (see, e.g., [13]).

### 96 2.1.1 B3 creep model

As the most popular, Bazant's B3 model with logarithmic-power law was used to describe concrete creep

$$J(t, t') = q_1 + q_2 Q(t, t') + q_3 \ln \left[ 1 + \left( \frac{t-t'}{\lambda_0} \right)^n \right] + q_4 \ln \left( \frac{t}{t'} \right), \quad (2.4)$$

97 where  $J(t, t')$  is the compliance function at time  $t$  due to a unit stress  $\sigma = 1$  applied at time  
 98  $t'$ . The material parameter  $q_1$  is the instantaneous strain due to unit stress. The term with  
 99 the coefficient  $q_2$  represents the ageing viscoelastic compliance,  $q_3$  non-ageing viscoelastic  
 100 compliance and  $q_4$  flow compliance. The coefficient  $\lambda_0$  is almost equal to 1.0 and  $Q(t, t')$   
 101 is a binomial integral. Detailed description of all coefficients can be found, e.g., in [3].

### 102 2.1.2 Moisture and temperature effect

103 Any model which has to describe concisely the behaviour of concrete structures exposed  
 104 to temperature and moisture changes should cover three complex phenomena in concrete  
 105 creep (solidification model [5]):

- 106 • The ageing of concrete, which is manifested by a significant decrease of creep with  
 107 the age at loading is of two types:

- 108       – Shorter-term chemical ageing, which ceases at room temperature after about a  
 109       year and is caused by the fact that new solids are produced by the slowly ad-  
 110       vancing chemical reactions of cement hydration and deposit (in an essentially  
 111       stress-free) on the walls of capillary pores.
- 112       – Long-term non-chemical ageing, manifested by the fact that the decrease of  
 113       creep with the age at loading continues unabated even for many years after  
 114       the degree of hydration of cement ceased to grow.
- 115       • The drying creep effect, also called the stress-induced shrinkage or Picket effect,  
 116       which is a transient effect consisting in the fact that the apparent creep during dry-  
 117       ing is much larger than the basic creep (i.e., creep at moisture saturation) while the  
 118       creep after drying (i.e., after reaching thermodynamical equilibrium with a reduced  
 119       environmental humidity) is much smaller than basic creep. It consists of an appar-  
 120       ent mechanism consisting of an apparent additional creep due to microcracking  
 121       and a true mechanism that resides in the nanostructure.
- 122       • The transitional creep, which represents a transient increase of creep after a temper-  
 123       ature change, both heating and cooling. In the case of cooling, the transient increase  
 124       is of the opposite sign than the final change in creep rate after a steady-state lower  
 125       temperature has been regained. Like the drying creep effect, this effect has two  
 126       analogous mechanisms [5]:
- 127       – An apparent macroscopic mechanism, due to thermally induced microcrack-  
 128       ing and similar to drying creep.
- 129       – A nanoscale mechanism due to a change in the level of microprestress caused  
 130       by a change of chemical potential of nanopore water with a temperature change.

131       The effect of temperature on concrete creep is twofold, generated by two different  
 132       mechanisms:

- 133       • A temperature increase accelerates the bond breakages and restorations causing  
 134       creep, and thus increases the creep rate.
- 135       • The higher the temperature, the faster is the chemical process of cement hydration  
 136       and thus the ageing of concrete, which reduces the creep rate.

137       Usually the former effect prevails and then the overall effect of temperature rise in an  
 138       increase of creep. The special time quantities are applied into creep model:

- Reduced time  $t_r$  characterizing the changes in the rate of bond breakages and restora-  
 tion on the microstructural level

$$t_r(t) = \int_0^t \psi(t') dt' \leq t, \quad (2.5)$$

where

$$\psi(t) = \psi_T(t)\psi_\varphi(t), \quad (2.6)$$

$$\psi_T(t) = \exp\left\{\frac{Q_v}{R}\left(\frac{1}{T_0} - \frac{1}{T}\right)\right\}, \quad (2.7)$$

$$\psi_\varphi(t) = \alpha_\varphi + (1 - \alpha_\varphi)\varphi^2(t), \quad (2.8)$$

139 where  $T$  is the absolute temperature,  $T_0$  is the reference temperature,  $\varphi$  is the relative  
140 humidity in the pores of cement paste,  $R$  is the gas constant,  $Q_v$  is the activation  
141 energy for the viscous processes and  $\alpha_\varphi$  is a material parameter that has to  
142 be determined experimentally. With respect to a large set of experiments, Bazant  
143 determined the following parameters  $T_0 = 294$  K,  $Q_v/R = 5000$  K and  $\alpha_\varphi = 0.1$ .

- Equivalent time  $t_e$  (equivalent hydration period or maturity), which indirectly characterizes the degree of hydration ( $t_e \geq t$ )

$$t_e(t) = \int_0^t \beta(t') dt', \quad (2.9)$$

where

$$\beta(t) = \beta_T(t)\beta_\varphi(t), \quad (2.10)$$

$$\beta_T(t) = \exp\left\{\frac{Q_h}{R}\left(\frac{1}{T_0} - \frac{1}{T}\right)\right\}, \quad (2.11)$$

$$\beta_\varphi(t) = \{1 + [a_\varphi - a_\varphi\varphi(t)]^4\}^{-1}, \quad (2.12)$$

144 where  $Q_h$  is the activation energy,  $Q_h/R = 2700$  K and  $a_\varphi = 5$ .

145 Moisture changes have the similar effect in ageing of concrete [5]. The rate of hydration  
146 and creep decrease with decreasing relative humidity  $\varphi$  and when  $\varphi$  approaches 0.3,  
147 the rate of ageing is almost zero.

148 The effect of temperature and humidity changes (structural thermal expansion and  
149 shrinkage) at zero stress can be expressed in strain rates:

- thermal expansion rate

$$\dot{\epsilon}_t = \alpha \dot{T} \Rightarrow \Delta \epsilon_t = \alpha \dot{T} \Delta t = \alpha \Delta T, \quad (2.13)$$

- drying shrinkage rate

$$\dot{\epsilon}_{sh} = k \dot{\varphi} \Rightarrow \Delta \epsilon_{sh} = k \dot{\varphi} \Delta t = k \Delta \varphi, \quad (2.14)$$

150 where  $k = \{k_{11}, k_{22}, k_{33}, k_{23}, k_{31}, k_{12}\}^T$  is the incremental shrinkage coefficient vector, which  
151 depends on  $\varphi$ ,  $T$  and  $t_e$ , and  $\alpha = \{\alpha_{11}, \alpha_{22}, \alpha_{33}, \alpha_{23}, \alpha_{31}, \alpha_{12}\}^T$  is the thermal expansion coef-  
152 ficient vector.

Providing the shrinkage and thermal expansion are independent of stress, they assume the form

$$\mathbf{k} = \varepsilon_{sh}^0 \psi \mathbf{m}, \quad \boldsymbol{\alpha} = \alpha^0 \mathbf{m}, \quad \mathbf{m} = \{1, 1, 1, 0, 0, 0\}^T, \quad (2.15)$$

153 where  $(-\varepsilon_{sh}^0) = 0.0002 \div 0.001$  and  $\alpha^0$  are empirical constants, and  $(-\psi) = E(t')/E(t_e)3\varphi^2$   
154 for  $0.4 \leq \varphi \leq 0.98$ .

In the presence of stress, the shrinkage and thermal expansion coefficient vectors are approximated as linear functions of the stress vector [4],  $\boldsymbol{\sigma} = \{\sigma_{11}, \sigma_{22}, \sigma_{33}, \sigma_{23}, \sigma_{31}, \sigma_{12}\}^T$  as

$$\mathbf{k} = \varepsilon_{sh}^0 \psi (\mathbf{m} + r \boldsymbol{\sigma} \text{sign}(\dot{H})), \quad \boldsymbol{\alpha} = \alpha^0 (\mathbf{m} + \rho \boldsymbol{\sigma} \text{sign}(\dot{H})), \quad (2.16)$$

155 where  $\dot{H} = \dot{\varphi} + c\dot{T}$  ( $c$  being a non-negative constant). Empirical coefficients normally at-  
156 tain the values  $r = (0.1 \div 0.6)/f'_t$  ( $\text{MPa}^{-1}$ ),  $\rho = (1 \div 2)/f'_t$  ( $\text{MPa}^{-1}$ ), where  $f'_t$  is the tensile  
157 strength. In [2], Eq. (2.16) are simplified by considering  $c \rightarrow 0$  in case of  $\mathbf{k}$ , to get  $\text{sign}(\dot{H}) =$   
158  $\text{sign}(\dot{\varphi})$ , and by setting  $c \rightarrow \infty$  in case of  $\boldsymbol{\alpha}$ , thus yielding  $\text{sign}(\dot{H}) = \text{sign}(\dot{T})$ . A general  
159 linear dependence (2.16) would also include terms proportional to  $\sigma_{\text{mean}} = \boldsymbol{\sigma}^T \mathbf{m}/3$ , which,  
160 however, seem to be negligible.

Generalization into 3D and including incremental form of shrinkage  $\Delta\varepsilon_{sh} = \mathbf{k}\Delta\varphi$  and thermal dilatation  $\Delta\varepsilon_t = \boldsymbol{\alpha}\Delta T$ , the incremental constitutive equation based on the Dirichlet-Prony series is obtained

$$\Delta\boldsymbol{\sigma} = \hat{E}_i \hat{D} (\Delta\varepsilon - \mathbf{k}\Delta\varphi - \boldsymbol{\alpha}\Delta T - \Delta\varepsilon_c - \Delta\varepsilon_d), \quad (2.17)$$

where

$$\hat{E}_i = \sum_{\mu=1}^M \frac{\bar{E}_\mu}{\Delta y_\mu} (1 - e^{-\Delta y_\mu}), \quad \text{with} \quad \bar{E}_\mu = \frac{1}{D_\mu}, \quad (2.18)$$

$$\hat{C} = \hat{D}^{-1} = \begin{pmatrix} 1 & -\nu & -\nu & 0 & 0 & 0 \\ & 1 & -\nu & 0 & 0 & 0 \\ & & 1 & 0 & 0 & 0 \\ & & & 2(1+\nu) & 0 & 0 \\ & & & & 2(1+\nu) & 0 \\ & & & & & 2(1+\nu) \end{pmatrix}. \quad (2.19)$$

## 161 2.2 Scalar isotropic damage model

162 Concrete belongs to quasi-brittle materials. In such materials, exceeding of a certain level  
163 of strains leads to evolution of defects such as microcracks and microvoids. If the evolu-  
164 tion of strains continues, the growth of defects localizes to some of them while evolution  
165 of the rest stops. The process is called as localization of inelastic strains. It can be de-  
166 scribed by a variety of models depending on the concept of yielding.

The scalar isotropic damage model is one of the simplest models of continuum damage mechanics. More details about the model can be found in [24] and [33]. The damage models consist in concepts of virgin, damaged and pseudo-undamaged states of material. The material is assumed to be at virgin state when no defects are present which corresponds to elastic state. Considering the one-dimensional case, the area of the cross-section of a bar element is denoted by  $A$  at the virgin state. The bar element is subjected to increasing uniaxial stress. Evolution of defects starts at a certain level of deformation. Let the area of these defects be denoted by  $A_d$ . In the damaged state, the nominal stress  $\sigma$  is assumed acting on the original cross-section area  $A$  while in the pseudo-undamaged state the effective stress  $\tilde{\sigma}$  acts on the undamaged area  $\tilde{A} = A - A_d$ . The equilibrium condition on the bar element can be written in the form

$$\sigma A = \tilde{\sigma} \tilde{A} \quad (2.20)$$

and dimensionless damage parameter  $\omega$  can be defined

$$\omega = \frac{A_d}{A}. \quad (2.21)$$

Using Eqs. (2.20) and (2.21), the stress-strain relation for the one-dimensional case can be written

$$\sigma = (1 - \omega) E \bar{\varepsilon}, \quad (2.22)$$

where  $\bar{\varepsilon}$  represents strain without irreversible strains in the form

$$\bar{\varepsilon} = \varepsilon - \varepsilon_p - \varepsilon_c - \varepsilon_{sh} - \varepsilon_t \quad (2.23)$$

and  $E$  is the Young modulus of elasticity. Eq. (2.22) can be rewritten to the form

$$\sigma = E(\bar{\varepsilon} - \varepsilon_d) = E \varepsilon_e, \quad (2.24)$$

where

$$\varepsilon_d = \omega \bar{\varepsilon}. \quad (2.25)$$

Additionally, the evolution law for damage parameter  $\omega$  has to be established and it depends on the type of the modelled material. In reference [28], the evolution law suitable for concrete was proposed in the form

$$\omega = \frac{a(\bar{\varepsilon} - \bar{\varepsilon}_0)^b}{1 + a(\bar{\varepsilon} - \bar{\varepsilon}_0)^b}, \quad (2.26)$$

167 where  $\bar{\varepsilon}_0$  is the strain threshold,  $a$  and  $b$  are material parameters controlling the peak  
168 value and slope of the softening branch. The damage evolves after the strains exceed the  
169 limit value of  $\bar{\varepsilon}_0$ .

It is known, [24], that damage models are mesh sensitive. It is connected with the dissipated energy which depends on the characteristic size of a damaged element and it



leads to physically unrealistic results. Dissipated energy tends to zero with decreasing characteristic size of the element. The so-called method of the variable softening modulus was developed, [30], in order to avoid the spurious mesh dependency. The method consists in involving of the characteristic element length into the damage evolution law. Assuming the one-dimensional case, the stress can be expressed in the form

$$\sigma = f_t \exp\left(-\frac{w_{cr}}{w_{cr0}}\right), \quad (2.27)$$

where  $f_t$  is the tensile strength in [Pa],  $w_{cr}$  is the crack opening in [m] and  $w_{cr0}$  is the material parameter controlling the initial slope of the softening branch in [m]. The crack opening can be smeared over the element using the following equation

$$\bar{\varepsilon} - \varepsilon_e = \frac{w_{cr}}{h}, \quad (2.28)$$

where  $h$  is the characteristic element length. When combining Eqs. (2.22), (2.28) and (2.27), the resulting non-linear equation for the damage parameter  $\omega$  yields

$$(1 - \omega)E\bar{\varepsilon} = f_t \exp\left(-\frac{\omega h \bar{\varepsilon}}{w_{cr0}}\right). \quad (2.29)$$

In the general three-dimensional case, the stress-strain relation can be obtained similarly in the form

$$\sigma = (1 - \omega)D_e \bar{\varepsilon}. \quad (2.30)$$

The damage parameter  $\omega$  is computed with help of the evolution law similar to the one-dimensional case where the strain  $\bar{\varepsilon}$  has to be substituted by equivalent strain  $\kappa$ . There are many definitions of the equivalent strain  $\kappa$  but in the case of concrete modelling, the most used definition is the Mazars' norm [27] which has the form

$$\kappa = \sqrt{\langle \bar{\varepsilon}_\alpha \rangle \langle \bar{\varepsilon}_\alpha \rangle}, \quad (2.31)$$

170 where  $\bar{\varepsilon}_\alpha$  denotes the principal values of the strain tensor  $\bar{\varepsilon}$  and the symbol  $\langle \rangle$  denotes  
171 selection of positive components (McAulley brackets).

### 172 2.3 Orthotropic damage model

173 The main drawback of the scalar isotropic damage model is that it uses only one damage  
174 parameter for all principle directions regardless of tension or compression. Once the  
175 damage parameter caused by exceeding limit strain in one principle direction evolves,  
176 it reduces stiffness in all remaining principle directions even though they should not be  
177 influenced. This drawback is not significant in the case of the one-dimensional stress state  
178 such as pure bending but it becomes more important especially for the three-dimensional  
179 stress state.

180 That led to development of the more advanced damage model which can describe  
 181 better the 3D problems. In reference [28], the authors proposed general anisotropic model  
 182 for concrete which contains nine material parameters. The laboratory measurements of  
 183 the required material parameters has to be performed but it caused difficulties for certain  
 184 cases. Additionally, the model required a significant number of internal variables that  
 185 have to be stored. These difficulties led to development of a simplified version of the  
 186 model which is based on six material parameters – three for tension and another three  
 187 parameters for compression.

The model is based on the following stress-strain relation

$$\sigma_\alpha = \left(1 - H(\bar{\varepsilon}_\alpha)D_\alpha^{(t)} - H(-\bar{\varepsilon}_\alpha)D_\alpha^{(c)}\right) \left[ \left(K - \frac{2}{3}G\right)\bar{\varepsilon}_v + 2G\bar{\varepsilon}_\alpha \right], \quad (2.32)$$

188 where the subscript  $\alpha$  stands for the index of principle components of the given quantity.  
 189 The model defines two sets of damage parameters  $D_\alpha^{(t)}$  and  $D_\alpha^{(c)}$  for tension and compres-  
 190 sion, respectively. In the equation (2.32), the symbol  $H()$  denotes the Heaviside function,  
 191  $K$  is the bulk modulus,  $G$  is the shear modulus and  $\bar{\varepsilon}_v$  stands for volumetric strain.

There are many evolution laws that can be used for  $D_\alpha^{(t)}$  and  $D_\alpha^{(c)}$  description. In our problems, the two evolution laws for the damage parameters are used similar to the laws used in the scalar isotropic damage model. The first law gives better results for compression but the determination of the material parameters is more complicated. It can be written in the form

$$D_\alpha^{(\beta)} = \frac{A^{(\beta)} \left( |\bar{\varepsilon}_\alpha^{(\beta)}| - \bar{\varepsilon}_0^{(\beta)} \right)^{B^{(\beta)}}}{1 + A^{(\beta)} \left( |\bar{\varepsilon}_\alpha^{(\beta)}| - \bar{\varepsilon}_0^{(\beta)} \right)^{B^{(\beta)}}}, \quad (2.33)$$

where the superscript  $(\beta)$  represents indices  $t$  or  $c$  which are used for tension and compression.  $A^{(\beta)}$ ,  $B^{(\beta)}$  and  $\bar{\varepsilon}_0^{(\beta)}$  are material parameters with the same meaning as in the similar law defined by (2.26). The second law involves correction of the dissipated energy with respect to the size of elements and it describes tension better. It is defined by the non-linear equation (2.34) which can be solved using the Newton method

$$\left(1 - D_\alpha^{(\beta)}\right) E |\bar{\varepsilon}_\alpha^{(\beta)}| = f_\beta \exp\left(-\frac{D_\alpha^{(\beta)} h |\bar{\varepsilon}_\alpha^{(\beta)}|}{w_{cr0}^{(\beta)}}\right). \quad (2.34)$$

192 In the above equation,  $f_\beta$  represents the tensile or compressive strength and  $w_{cr0}^{(\beta)}$  controls  
 193 the initial slope of the softening branches. More details about the implemented models  
 194 can be found in [16–18].

### 195 3 Heat and moisture transfer

196 Transport of heat and moisture in porous medium can be assumed by convection, dif-  
197 fusion or their combination. In all cases, three types of equations have to be solved.  
198 The transport equations express fluxes with respect to gradients of unknown variables.  
199 The constitutive equations define relationships between unknown variables and internal  
200 variables. As an example can serve the retention curves, sorption isotherms, etc. Finally,  
201 the third set of equations contains the balance (conservation) equations. Gradual sub-  
202 stitution of the constitutive equations to the transport equations and then to the balance  
203 equations leads to the governing equations. The governing equations are partial differ-  
204 ential equations and they have to be solved numerically. After spatial discretization of  
205 governing equations using the finite element method and after temporal discretization  
206 by the generalized trapezoidal method, the system of non-symmetric and non-linear al-  
207 gebraic equations is obtained.

208 One of the most popular models is summarized in this paper. It is the Künzel and  
209 Kiessl's phenomenological model [23] based on the diffusion theory. This model is suit-  
210 able for numerical simulations of building structures under common climatic condi-  
211 tions. Other models and description of climatic conditions can be found in references  
212 [6, 10, 14, 15, 25, 29].

#### 213 3.1 Künzel and Kiessl's coupled heat and moisture transfer approach

214 The model introduces two unknowns in a material point, relative humidity  $\varphi$  [-] and tem-  
215 perature  $T$  [K]. The model divides overhygroscopic region into two subranges – capillary  
216 water region and supersaturated region, where different conditions for water and water  
217 vapour transport are considered. For the description of simultaneous water and water  
218 vapour transport, the relative humidity  $\varphi$  is chosen as the only moisture potential for  
219 both hygroscopic and overhygroscopic range. This model uses certain simplifications.  
220 Nevertheless, proposed model describes all substantial phenomena and the predicted re-  
221 sults comply well with experimentally obtained data, which is the main advantage of the  
222 model together with easy and quick determination of the material properties measured  
223 in a laboratory.

##### 224 3.1.1 Transport equations

225 Künzel proposed that the moisture transport mechanisms relevant to numerical analysis  
226 in the field of building physics are just water vapour diffusion and liquid transport [23].  
227 Vapour diffusion is the most important in large pores, whereas liquid transport takes  
228 place on pore surfaces and in small capillaries.

Vapour diffusion in porous media is described in the model by the Fick's diffusion  
and effusion in the form

$$J_v = -\delta_p \nabla p = -\frac{\delta}{\mu} \nabla p, \quad (3.1)$$

229 where  $J_v$  is the water vapour flux,  $\delta_p$  [ $\text{kg m}^{-1} \text{s}^{-1} \text{Pa}^{-1}$ ] is the vapour permeability of the  
 230 porous material,  $p$  denotes vapour pressure [Pa], the vapour diffusion resistance number  
 231  $\mu$  is a material property and  $\delta$  [ $\text{kg m}^{-1} \text{s}^{-1} \text{Pa}^{-1}$ ] is the vapour diffusion coefficient in the  
 232 air.

The liquid transport mechanism includes liquid flow in the absorbed layer (surface diffusion) and in the water filled capillaries (capillary transport). The driving potential in both cases is capillary pressure (suction stress) or relative humidity  $\varphi$ . The flux of liquid water is described by

$$J_w = -D_\varphi \nabla \varphi, \quad (3.2)$$

233 where the liquid conductivity  $D_\varphi$  [ $\text{kg m s}^{-1}$ ] is the product of the liquid diffusivity  $D_w$   
 234 [ $\text{m}^2 \text{s}^{-1}$ ] and the derivative of water retention function  $D_\varphi = D_w \cdot dw/d\varphi$ .

The heat flux is proportional to the thermal conductivity of the moist porous material and the temperature gradient (Fourier's law)

$$q = -\lambda \nabla T, \quad (3.3)$$

235 where  $\lambda$  [ $\text{W m}^{-1} \text{K}^{-1}$ ] is the thermal conductivity of the moist material. The enthalpy  
 236 flows through moisture movement and phase transition is taken into account in the form  
 237 of source terms in the heat balance equation.

### 238 3.1.2 Balance equations

The heat and moisture balance equations are closely coupled because the moisture content depends on the total enthalpy and thermal conductivity while the temperature depends on moisture flow. The resulting set of differential equations for the description of simultaneous heat and moisture transfer, expressed in terms of temperature  $T$  and relative humidity  $\varphi$ , have the form of partial differential equations defined on a domain  $\Omega$

$$\frac{dw}{d\varphi} \frac{\partial \varphi}{\partial t} = \nabla^T (D_\varphi \nabla \varphi + \delta_p \nabla (\varphi p_{\text{sat}})), \quad x \in \Omega, \quad (3.4)$$

$$\left( \rho C + \frac{dH_w}{dT} \right) \frac{\partial T}{\partial t} = \nabla^T (\lambda \nabla T) + h_v \nabla^T (\delta_p \nabla (\varphi p_{\text{sat}})), \quad x \in \Omega, \quad (3.5)$$

239 where  $H_w$  [ $\text{J m}^{-3}$ ] is the enthalpy of the material moisture,  $w$  [ $\text{kg m}^{-3}$ ] is the water con-  
 240 tent of the material,  $h_v$  [ $\text{J kg}^{-1}$ ] is the evaporation enthalpy of the water,  $p_{\text{sat}}$  [Pa] is the  
 241 water vapour saturation pressure,  $\rho$  [ $\text{kg m}^{-3}$ ] is the material density,  $C$  [ $\text{J kg}^{-1} \text{K}^{-1}$ ] is the  
 242 specific heat capacity and  $t$  [s] denotes time. Boundary of the domain  $\Omega$  is split into parts  
 243  $\Gamma_T$ ,  $\Gamma_\varphi$ ,  $\Gamma_{qpT}$ ,  $\Gamma_{Jp\varphi}$ ,  $\Gamma_{qcT}$  and  $\Gamma_{Jc\varphi}$ . The parts  $\Gamma_T$ ,  $\Gamma_{qpT}$  and  $\Gamma_{qcT}$  are disjoint and their union is  
 244 the whole boundary  $\Gamma$ . The same is valid for the parts  $\Gamma_\varphi$ ,  $\Gamma_{Jp\varphi}$  and  $\Gamma_{Jc\varphi}$ . The heat fluxes  
 245 are prescribed on the part  $\Gamma_q = \Gamma_{qpT} \cup \Gamma_{qcT}$  and the moisture fluxes are prescribed on the  
 246 part  $\Gamma_J = \Gamma_{Jp\varphi} \cup \Gamma_{Jc\varphi}$ .

### 247 3.1.3 Initial and Boundary conditions

248 The system of equations (3.4) and (3.5) are accompanied with three types of boundary  
249 conditions:

- Dirichlet boundary conditions

$$T(\mathbf{x}, t) = \bar{T}(\mathbf{x}, t), \quad \mathbf{x} \in \Gamma_T, \quad (3.6)$$

$$\varphi(\mathbf{x}, t) = \bar{\varphi}(\mathbf{x}, t), \quad \mathbf{x} \in \Gamma_\varphi, \quad (3.7)$$

- Neumann boundary conditions

$$\mathbf{q}(\mathbf{x}, t) = \bar{\mathbf{q}}(\mathbf{x}, t), \quad \mathbf{x} \in \Gamma_{qpT}, \quad (3.8)$$

$$\mathbf{J}(\mathbf{x}, t) = \bar{\mathbf{J}}(\mathbf{x}, t), \quad \mathbf{x} \in \Gamma_{Jp\varphi}, \quad (3.9)$$

- Cauchy boundary conditions

$$\mathbf{q}(\mathbf{x}, t) = \beta_T(T(\mathbf{x}, t) - T_\infty(\mathbf{x}, t)), \quad \mathbf{x} \in \Gamma_{qcT}, \quad (3.10)$$

$$\mathbf{J}(\mathbf{x}, t) = \beta_\varphi(p(\mathbf{x}, t) - p_\infty(\mathbf{x}, t)), \quad \mathbf{x} \in \Gamma_{Jc\varphi}, \quad (3.11)$$

where  $\bar{T}(\mathbf{x}, t)$  is the prescribed temperature,  $\bar{\varphi}(\mathbf{x}, t)$  is the prescribed relative humidity,  $\bar{\mathbf{q}}(\mathbf{x}, t)$  is the prescribed heat flux,  $\bar{\mathbf{J}}(\mathbf{x}, t)$  is the prescribed moisture flux,  $\beta_T$  [ $\text{W m}^{-2} \text{K}^{-1}$ ] and  $\beta_\varphi$  [ $\text{kg s}^{-1} \text{Pa}^{-1}$ ] are the heat and mass transfer coefficient,  $T_\infty$  is the ambient temperature and  $p_\infty$  is the ambient water vapour pressure. Besides the boundary conditions, the initial conditions are prescribed, i.e.

$$T(\mathbf{x}, 0) = T_0(\mathbf{x}), \quad \mathbf{x} \in \Omega, \quad (3.12)$$

$$\varphi(\mathbf{x}, 0) = \varphi_0(\mathbf{x}), \quad \mathbf{x} \in \Omega, \quad (3.13)$$

250 where  $T_0(\mathbf{x})$  denotes the initial temperature and  $\varphi_0(\mathbf{x})$  denotes the initial relative humid-  
251 ity.

### 252 3.1.4 Discretization of the differential equations

The finite element method is used for spatial discretization of the partial differential equations (3.4) and (3.5). The weighted residual statement is applied to the mass balance equation assuming  $\delta T = 0$  on  $\Gamma_T$  and  $\delta \varphi = 0$  on  $\Gamma_\varphi$

$$\int_{\Omega} \delta \varphi \left( \frac{dw}{d\varphi} \frac{\partial \varphi}{\partial t} - \nabla^T (D_\varphi \nabla \varphi + \delta_p \nabla (\varphi p_{\text{sat}})) \right) d\Omega = 0 \quad (3.14)$$

and also to the energy balance equation

$$\int_{\Omega} \delta T \left( (\rho C + \frac{dH_w}{dT}) \frac{\partial T}{\partial t} - \nabla^T (\lambda \nabla T) - h_v \nabla^T (\delta_p \nabla (\varphi p_{\text{sat}})) \right) d\Omega = 0. \quad (3.15)$$

Applying Green's theorem the weak formulation for the mass transfer yields

$$\begin{aligned} \int_{\Omega} \delta\varphi \left( \frac{dw}{d\varphi} \frac{\partial\varphi}{\partial t} \right) d\Omega + \int_{\Omega} \nabla(\delta\varphi) \left( D_w \frac{dw}{d\varphi} + \delta_p p_{\text{sat}} \right) \nabla\varphi d\Omega + \int_{\Omega} \nabla(\delta\varphi) \left( \delta_p \varphi \frac{dp_{\text{sat}}}{dT} \right) \nabla T d\Omega \\ - \int_{\Gamma_j} \delta\varphi \left( D_w \frac{dw}{d\varphi} + \delta_p p_{\text{sat}} \right) \frac{\partial\varphi}{\partial \mathbf{n}} d\Gamma - \int_{\Gamma_q} \delta\varphi \left( \delta_p \varphi \frac{dp_{\text{sat}}}{dT} \right) \frac{\partial T}{\partial \mathbf{n}} d\Gamma = 0 \end{aligned} \quad (3.16)$$

and the weak formulation for heat transfer

$$\begin{aligned} \int_{\Omega} \delta T \left( \rho C + \frac{dH_w}{dT} \right) \frac{\partial T}{\partial t} d\Omega + \int_{\Omega} \nabla(\delta T) \left( \lambda + h_v \delta_p \varphi \frac{dp_{\text{sat}}}{dT} \right) \nabla T d\Omega \\ + \int_{\Omega} \nabla(\delta T) \left( h_v \delta_p p_{\text{sat}} \right) \nabla\varphi d\Omega - \int_{\Gamma_j} \delta T \left( h_v \delta_p p_{\text{sat}} \right) \frac{\partial\varphi}{\partial \mathbf{n}} d\Gamma \\ - \int_{\Gamma_q} \delta T \left( \lambda + h_v \delta_p \varphi \frac{dp_{\text{sat}}}{dT} \right) \frac{\partial T}{\partial \mathbf{n}} d\Gamma = 0. \end{aligned} \quad (3.17)$$

In the finite element method, the temperature  $T$  and relative humidity  $\varphi$  are approximated in the form

$$T = \mathbf{N}(\mathbf{x}) \mathbf{d}_T, \quad \varphi = \mathbf{N}(\mathbf{x}) \mathbf{d}_{\varphi} \quad (3.18)$$

and the gradients of temperature and relative humidity are also needed

$$\nabla T = \mathbf{B}(\mathbf{x}) \mathbf{d}_T, \quad \nabla\varphi = \mathbf{B}(\mathbf{x}) \mathbf{d}_{\varphi}. \quad (3.19)$$

In the previous equations,  $\mathbf{N}(\mathbf{x})$  denotes the matrix of approximation functions,  $\mathbf{B}(\mathbf{x})$  is the matrix of their derivatives,  $\mathbf{d}_T$  denotes the vector of nodal temperatures and  $\mathbf{d}_{\varphi}$  denotes the vector of nodal relative humidities. Using approximations (3.18) and (3.19) in Eqs. (3.16) and (3.17), a set of the first order differential equations is obtained in the matrix form

$$\begin{pmatrix} \mathbf{K}_{\varphi\varphi} & \mathbf{K}_{\varphi T} \\ \mathbf{K}_{T\varphi} & \mathbf{K}_{TT} \end{pmatrix} \begin{pmatrix} \mathbf{d}_{\varphi} \\ \mathbf{d}_T \end{pmatrix} + \begin{pmatrix} \mathbf{C}_{\varphi\varphi} & \mathbf{C}_{\varphi T} \\ \mathbf{C}_{T\varphi} & \mathbf{C}_{TT} \end{pmatrix} \begin{pmatrix} \dot{\mathbf{d}}_{\varphi} \\ \dot{\mathbf{d}}_T \end{pmatrix} = \begin{pmatrix} \mathbf{J}_{\varphi} \\ \mathbf{q}_T \end{pmatrix}. \quad (3.20)$$

The matrices  $\mathbf{K}_{\varphi\varphi}$ ,  $\mathbf{K}_{\varphi T}$ ,  $\mathbf{K}_{T\varphi}$  and  $\mathbf{K}_{TT}$  create the conductivity matrix of the problem and they have the form

$$\mathbf{K}_{\varphi\varphi} = \int_{\Omega} \mathbf{B}^T \mathbf{D}_{\varphi\varphi} \mathbf{B} d\Omega, \quad \mathbf{K}_{\varphi T} = \int_{\Omega} \mathbf{B}^T \mathbf{D}_{\varphi T} \mathbf{B} d\Omega, \quad (3.21)$$

$$\mathbf{K}_{T\varphi} = \int_{\Omega} \mathbf{B}^T \mathbf{D}_{T\varphi} \mathbf{B} d\Omega, \quad \mathbf{K}_{TT} = \int_{\Omega} \mathbf{B}^T \mathbf{D}_{TT} \mathbf{B} d\Omega, \quad (3.22)$$

where the conductivity matrices of material  $\mathbf{D}_{\varphi\varphi}$ ,  $\mathbf{D}_{\varphi T}$ ,  $\mathbf{D}_{T\varphi}$  and  $\mathbf{D}_{TT}$  are diagonal matrices and the diagonal entries are equal to appropriate conductivities

$$k_{\varphi\varphi} = D_w \frac{dw}{d\varphi} + \delta_p p_{\text{sat}}, \quad k_{\varphi T} = \delta_p \varphi \frac{dp_{\text{sat}}}{dT}, \quad (3.23)$$

$$k_{T\varphi} = h_v \delta_p p_{\text{sat}}, \quad k_{TT} = \lambda + h_v \delta_p \varphi \frac{dp_{\text{sat}}}{dT}. \quad (3.24)$$

The matrices  $C_{\varphi\varphi}$ ,  $C_{\varphi T}$ ,  $C_{T\varphi}$  and  $C_{TT}$  create the capacity matrix of the problem and they have the form

$$C_{\varphi\varphi} = \int_{\Omega} N^T H_{\varphi\varphi} N d\Omega, \quad C_{\varphi T} = \int_{\Omega} N^T H_{\varphi T} N d\Omega, \quad (3.25)$$

$$C_{T\varphi} = \int_{\Omega} N^T H_{T\varphi} N d\Omega, \quad C_{TT} = \int_{\Omega} N^T H_{TT} N d\Omega, \quad (3.26)$$

where capacity matrices of material  $H_{\varphi\varphi}$ ,  $H_{\varphi T}$ ,  $H_{T\varphi}$  and  $H_{TT}$  are diagonal matrices and the diagonal entries are equal to appropriate capacities

$$c_{\varphi\varphi} = \frac{dw}{d\varphi}, \quad c_{\varphi T} = 0, \quad (3.27)$$

$$c_{T\varphi} = 0, \quad c_{TT} = \rho C + \frac{dH_w}{dT}. \quad (3.28)$$

The vectors  $J_{\varphi}$  and  $q_T$  contain prescribed nodal fluxes and have the form

$$J_{\varphi} = \int_{\Gamma_J} N^T \bar{J}_{\varphi} d\Gamma, \quad q_T = \int_{\Gamma_q} N^T \bar{q}_T d\Gamma, \quad (3.29)$$

253 where  $\bar{J}_{\varphi}$  denotes the mass boundary fluxes and  $\bar{q}_T$  denotes the heat boundary fluxes.

## 254 4 Numerical solution

255 From the numerical point of view, coupled problems are described by balance equations  
 256 which have the form of partial differential equations. The exact solution cannot be ob-  
 257 tained with respect to non-linearities hidden in the material models. Another obstacle is  
 258 caused by very general domains which are solved in real engineering problems. There-  
 259 fore, numerical methods have to be used.

The spatial discretization of the balance equations is done by the finite element method [7] and a system of ordinary differential equations with time variables is obtained. In the case of hydro-thermo-mechanical problem, the system may have the form

$$\begin{aligned} & \begin{pmatrix} C_{uu} & C_{uT} & C_{u\varphi} \\ C_{Tu} & C_{TT} & C_{T\varphi} \\ C_{\varphi u} & C_{\varphi T} & C_{\varphi\varphi} \end{pmatrix} \begin{pmatrix} \dot{d}_u \\ \dot{d}_T \\ \dot{d}_{\varphi} \end{pmatrix} + \begin{pmatrix} K_{uu} & K_{uT} & K_{u\varphi} \\ K_{Tu} & K_{TT} & K_{T\varphi} \\ K_{\varphi u} & K_{\varphi T} & K_{\varphi\varphi} \end{pmatrix} \begin{pmatrix} d_u \\ d_T \\ d_{\varphi} \end{pmatrix} \\ & = \begin{pmatrix} f_u \\ f_T \\ f_{\varphi} \end{pmatrix} = \begin{pmatrix} f_{uu} + f_{uT} + f_{u\varphi} \\ f_{Tu} + f_{TT} + f_{T\varphi} \\ f_{\varphi u} + f_{\varphi T} + f_{\varphi\varphi} \end{pmatrix}, \end{aligned} \quad (4.1)$$

260 where the subscript  $u$  denotes the displacements, the subscript  $\varphi$  denotes the relative  
 261 humidity and the subscript  $T$  denotes the temperature. The vectors  $d_u$ ,  $d_T$  and  $d_{\varphi}$  denote

262 unknown nodal variables, the vectors  $f_u$ ,  $f_T$  and  $f_\varphi$  denote prescribed nodal forces and  
 263 fluxes (usually denoted  $g$  and  $q$  in transport processes, see Eq. (3.29)), the matrices  $K$  with  
 264 subscripts denote the stiffness, conductivity and coupling matrices and the matrices  $C$   
 265 with subscripts denote the capacity and coupling matrices. The vectors  $f_u$ ,  $f_T$  and  $f_\varphi$  are  
 266 further split to three contributions. The vector  $f_u$  is the sum of vectors  $f_{uu}$ ,  $f_{uT}$  and  $f_{u\varphi}$   
 267 which represent contributions to the nodal forces from mechanical analysis, temperature  
 268 changes and humidity changes. The meaning of other contributions is similar.

The system of differential equations (4.1) can be written more compactly in the form

$$C(d)\dot{d} + K(d)d = f, \quad (4.2)$$

269 where the dependency of the stiffness, conductivity, capacity and coupling matrices on  
 270 the attained values of variables is explicitly denoted.  $\Delta d$  and  $\Delta \dot{d}$  denote increments of  
 271 nodal variables and their time derivatives.

The system (4.2) has to be solved by an incremental method. Time discretization is based on the v-form of the generalized trapezoidal method [12] defined by the relationships

$$d_{n+1} = d_n + \Delta t v_{n+\gamma}, \quad (4.3)$$

$$v_{n+\gamma} = (1-\gamma)v_n + \gamma v_{n+1}, \quad (4.4)$$

272 where  $v$  denotes the first derivatives of nodal values with respect to time and  $\gamma$  is a  
 273 parameter from the range  $[0,1]$ . The subscript  $n$  denotes the time step and it serves also  
 274 as an index in the incremental method, called the outer iteration loop. It is assumed that  
 275 all variables are known at the time  $t_n$  and variables at the time  $t_{n+1}$  are searched.

Substitution of expressions defined in Eqs. (4.3) and (4.4) to the system of differential equations (4.2) leads to relationship

$$(C_n + \Delta t \gamma K_n) v_{n+1} = f_{n+1} - K_n (d_n + \Delta t (1-\gamma) v_n), \quad (4.5)$$

276 where  $C_n$  and  $K_n$  denote the capacity and stiffness/conductivity matrices evaluated with  
 277 the help of values  $d_n$ . The system of algebraic equations (4.5) is generally non-linear and  
 278 the Newton-Raphson method [7, 8] has to be used at each time step.

The trial solution  $v_{n+1,0}$  of the system of equations (4.5) is used for computation of the trial nodal values  $d_{n+1,0}$  which are obtained from Eqs. (4.4) and (4.3). Substitution of the trial solution back to the system of equations (4.5) with modified matrices does not generally lead to equality. An iteration loop, called the inner iteration loop, in every time step is based on residual which is computed from the relationship

$$r_{n+1,j} = f_{n+1} - K_n (d_n + \Delta t (1-\gamma) v_n) - (C_{n+1,j} + \Delta t \gamma K_{n+1,j}) v_{n+1,j}, \quad (4.6)$$

where  $C_{n+1,j}$  and  $K_{n+1,j}$  denote the matrices evaluated for  $d_{n+1,j}$  and  $j$  is the index in the inner loop. Correction of nodal time derivatives are computed from the equation

$$(C_{n+1,j} + \Delta t \gamma K_{n+1,j}) \Delta v_{n+1,j+1} = r_{n+1,j} \quad (4.7)$$



and new time derivatives are in the form

$$\boldsymbol{v}_{n+1,j+1} = \boldsymbol{v}_{n+1,j} + \Delta t \boldsymbol{v}_{n+1,j+1}. \quad (4.8)$$

279 It has to be noted that the permanent recalculation of matrices  $\boldsymbol{K}$  and  $\boldsymbol{C}$  with respect  
 280 to actual nodal values is very computationally demanding. In such a case, the matrix  
 281 of the system of equations  $\boldsymbol{C}(\boldsymbol{d}) + \Delta t \gamma \boldsymbol{K}(\boldsymbol{d})$  has to be always factorized and it requires  
 282 additional computational time. The numerical examples show that the modified Newton  
 283 method, which changes the system matrix only at the beginning of a new time step is the  
 284 best choice.

## 285 5 Implementation

286 Implementation of numerical methods, material models and tools for parallel computing  
 287 has to satisfy several contradicting requirements. Easy extensibility of a code is proba-  
 288 bly the most important requirement. Another important requirement is connected with  
 289 code performance. These two basic requirements on a code are definitely contradictory  
 290 because really very efficient implementation of a numerical method differs significantly  
 291 from description of the method in textbooks and therefore the orientation in the code is  
 292 much more difficult.

The computer code SIFEL developed at our department is written in the C++ lan-  
 guage and can be found at the web address [32]. The attention is not concentrated on  
 particular programming language but rather on suitable formulation of the problem and  
 correct analysis. Detailed analysis of a system of non-linear ordinary differential equa-  
 tions (4.1) reveals similarity of particular submatrices. The stiffness and conductivity  
 matrices (denoted by  $\boldsymbol{K}$  with appropriate subscripts) have generally the form

$$\boldsymbol{K}_{ij} = \int_{\Omega} \boldsymbol{B}_i^T \boldsymbol{D}_{ij} \boldsymbol{B}_j d\Omega, \quad (5.1)$$

where  $\boldsymbol{B}_i$  and  $\boldsymbol{B}_j$  denote the gradient matrices,  $\boldsymbol{D}_{ij}$  denotes the matrix of stiffness or con-  
 ductivity of the material and the subscripts  $i$  and  $j$  substitute any of subscripts  $u$ ,  $T$  or  $\varphi$ .  
 Similarly, the capacity matrices (denoted by  $\boldsymbol{C}$  with appropriate subscripts) have gener-  
 ally the form

$$\boldsymbol{C}_{ij} = \int_{\Omega} \boldsymbol{N}_i^T \boldsymbol{H}_{ij} \boldsymbol{N}_j d\Omega, \quad (5.2)$$

293 where  $\boldsymbol{N}_i$  and  $\boldsymbol{N}_j$  denote the matrices of base functions and  $\boldsymbol{H}_{ij}$  denotes the matrix of  
 294 material parameters.

For better understanding, the following extension of the mechanical analysis is pre-  
 sented. Let an elastic material be assumed. The constitutive equation (Hook's law) has  
 the form

$$\boldsymbol{\sigma} = \boldsymbol{D}_{uu} \boldsymbol{\varepsilon}(\boldsymbol{u}) \quad (5.3)$$

and it relates the strains  $\boldsymbol{\varepsilon}(\boldsymbol{u})$  and stresses  $\boldsymbol{\sigma}$ .  $\boldsymbol{D}_{uu}$  is the stiffness matrix of the material. It should be noted that the strains depend on displacements  $\boldsymbol{u}$  which are discretized and the nodal displacements are denoted by  $\boldsymbol{d}_u$ . The mechanical problem with negligible inertial forces can be written in the form

$$\boldsymbol{K}_{uu}\boldsymbol{d}_u = \boldsymbol{f}_u, \quad (5.4)$$

295 where  $\boldsymbol{K}_{uu}$  denotes the stiffness matrix of structure and  $\boldsymbol{f}_u$  denotes the vector of pre-  
296 scribed nodal forces. Eq. (5.4) expresses the equilibrium condition.

If the temperature plays a role, the constitutive relationship (5.3) has to be replaced by the following constitutive equation

$$\boldsymbol{\sigma} = \boldsymbol{D}_{uu}\boldsymbol{\varepsilon}(\boldsymbol{u}) + \boldsymbol{D}_{uT}\nabla T, \quad (5.5)$$

where  $T$  is the temperature and  $\boldsymbol{D}_{uT}$  denotes the matrix of material coefficients. Moreover, the constitutive relationship between the heat flux  $\boldsymbol{q}$  and the temperature gradient is needed and it has the form

$$\boldsymbol{q} = \boldsymbol{D}_{TT}\nabla T, \quad (5.6)$$

where  $\boldsymbol{D}_{TT}$  is the conductivity matrix of material. It is usually accepted that the heat flux is independent of the displacements  $\boldsymbol{u}$ . The equilibrium condition (5.4) is therefore extended with the heat balance equation and the system of equations has the form

$$\begin{pmatrix} \boldsymbol{K}_{uu} & \boldsymbol{K}_{uT} \\ \mathbf{0} & \boldsymbol{K}_{TT} \end{pmatrix} \begin{pmatrix} \boldsymbol{d}_u \\ \boldsymbol{d}_T \end{pmatrix} = \begin{pmatrix} \boldsymbol{f}_u \\ \boldsymbol{f}_T \end{pmatrix}, \quad (5.7)$$

297 where  $\boldsymbol{d}_T$  is the vector of nodal temperatures and  $\boldsymbol{f}_T$  is the vector of prescribed nodal heat  
298 fluxes. The first equation in the system (5.7) expresses the equilibrium condition while  
299 the second equation in the system (5.7) expresses the heat balance condition. The zero  
300 block in the heat balance equation determines the independence of the heat transfer on  
301 the mechanical problem but on the contrary, the mechanical problem is coupled with the  
302 heat transfer.

303 Additional variables can be introduced in the constitutive equations and additional  
304 balance equations can be added to the system. The thermo-mechanical problem (5.7)  
305 extended by the relative humidity and capacity terms result in the form (4.1).

306 The previous analysis of the structure of system (4.1) offers directly the instruction for  
307 efficient implementation. Our implementation of the coupled hydro-thermo-mechanical  
308 problems is based on three independent modules. The first module, MEFEL, is an in-  
309 dependent computer code for mechanical analysis which can stand alone. It means, the  
310 code is able to deal with the pure mechanical analysis. It assembles submatrix  $\boldsymbol{K}_{uu}$  and  
311 subvector  $\boldsymbol{f}_{uu}$  from system (4.1). The second module, TRFEL, is an independent com-  
312 puter code for heat and moisture transfer which can also be used separately. It assembles  
313 the submatrices  $\boldsymbol{K}_{TT}$ ,  $\boldsymbol{K}_{T\varphi}$ ,  $\boldsymbol{K}_{\varphi T}$ ,  $\boldsymbol{K}_{\varphi\varphi}$ ,  $\boldsymbol{C}_{TT}$ ,  $\boldsymbol{C}_{T\varphi}$ ,  $\boldsymbol{C}_{\varphi T}$ ,  $\boldsymbol{C}_{\varphi\varphi}$  and subvectors  $\boldsymbol{f}_{TT}$ ,  $\boldsymbol{f}_{T\varphi}$ ,  $\boldsymbol{f}_{\varphi T}$ ,

314  $f_{\varphi\varphi}$ . The coupling between the mechanical and transport part is implemented in the  
315 third module, METR, which deals with the off-diagonal terms in the coupled problem.  
316 It means, this module assembles the submatrices  $K_{uT}$ ,  $K_{u\varphi}$ ,  $K_{Tu}$ ,  $K_{\varphi u}$ ,  $C_{uT}$ ,  $C_{u\varphi}$ ,  $C_{Tu}$ ,  $C_{\varphi u}$   
317 and the subvectors  $f_{uT}$ ,  $f_{u\varphi}$ ,  $f_{Tu}$  and  $f_{\varphi u}$ .

318 At this time, many concepts of merging software especially based on Python language  
319 can be found in literature. These concepts combine the existing computer codes and the  
320 exchange data among them. Unfortunately, a fully coupled analysis cannot be attained by  
321 these concepts. They result in staggered algorithms. In our concept, we do not merge the  
322 whole codes but we are using suitable subroutines from particular codes. The coupled  
323 problems are solved by the third module, METR, which uses many subroutines from the  
324 MEFEL and TRFEL codes. Of course, new subroutines dealing with the coupling terms  
325 had to be implemented. For better understanding, the numbers of lines of the source code  
326 are summarized. The MEFEL code contains approximately 210,000 lines, the TRFEL code  
327 contains 120,000 lines and the METR code contains 30,000 lines. It is clear that the number  
328 of lines of source code in METR is larger than is the usual number of lines in the Python  
329 merging code. On the other hand, it enables staggered as well as fully coupled analysis  
330 and the resulting code is compiled and therefore very fast.

331 Additional advantage stems from the fact that any improvement of the mechanical or  
332 transport module is automatically projected to the code for coupled problems. It is also  
333 very convenient for developers which can deal with one part of the whole code.

334 Modelling of the sequential construction of a structure is another important require-  
335 ment on the software for civil engineering problems. There are many possibilities for  
336 implementation of this feature. Some programs use a transfer of results from the mesh  
337 of the calculated stage to the next one via files but SIFEL uses more efficient implemen-  
338 tation. The mesh is generated for all construction stages at once and individual parts of  
339 the mesh are switched on and off by the state time functions specified for each element.  
340 Changes in the state of elements are monitored in the course of time and if there is a  
341 change, the nodal degrees of freedom are renumbered automatically.

342 The program can solve stationary and non-stationary, linear and non-linear problems  
343 of heat and moisture transfer as well as linear and non-linear statics, eigenvibrations,  
344 dynamics and time dependent problems with negligible inertial forces. A 2D and 3D  
345 domain can be modeled by various types of finite elements. The SIFEL has implemented  
346 the bar, triangular, quadrilateral, tetrahedron and hexahedron elements where both types  
347 of approximation functions, linear and quadratic, can be used.

## 348 5.1 Material models

349 The matrices defined by (5.1) and (5.2) are assembled with respect to the used material  
350 models. The proper selection of a material model is the key point in the analyses of  
351 real engineering and scientific problems. The implementation of material models con-  
352 sists in writing several functions connected with the evaluation of the material matrices  
353 and stresses or fluxes. There is no need for rewriting the other module parts such as

354 the routines dealing with elements. It can be demonstrated on the implementation of  
355 a new mechanical material model. In such a case, the user have to write the following  
356 procedures containing:

- 357 • reading of material parameters,
- 358 • assembling of the material stiffness matrix,
- 359 • computation of the stresses from the given strains,
- 360 • update of internal variables of the material model.

361 Both the modules TRFEL and MEFEL contain a number of material models. Many of  
362 them describe behaviour of concrete or soils because our team is focused on civil engi-  
363 neering problems where these materials play an important role.

364 The models implemented in MEFEL can be split into several main categories such as  
365 plasticity (J2 flow, Drucker-Prager, Mohr-Coulomb, Cam-Clay, HISS and Chen models),  
366 damage (scalar isotropic, orthotropic and anisotropic damage models), creep (Bazant's  
367 B3, simple viscoplasticity) and other (Microplane M4).

368 In the TRFEL module, there are implemented several material models, approaches  
369 and theories for heat transfer, moisture transfer, coupled heat and moisture transport,  
370 coupled heat-moisture and salt transport with phenomenological based models (Künzel  
371 and Kiessl, Grunewald, Pedersen) and micromechanical based models (Lewis and Schre-  
372 fler, Tenchev). Various types of sorption isotherms and moisture storage functions are  
373 also implemented (Root, Hansen, Bazant, Baroghel-Bouny), functions for experimentally  
374 measured data and non-linear behaviour of material parameters (heat conductivity, ca-  
375 pacity, permeability, etc.) The code allows to describe different types of boundary and  
376 initial conditions, e.g. Dirichlet boundary conditions (prescribed temperature, moisture,  
377 relative humidity, etc.), Neumann b. c. (prescribed fluxes of heat and mass), Cauchy b.  
378 c. (heat transfer on boundary, diffusion effect), climatic conditions exposure (wind effect,  
379 rain, water contact, heat transfer and moisture diffusion, short and long wave radiation)  
380 and the heat source condition, e.g. measured data from calorimetry, multiscale modelling  
381 of cement hydration process based on the model CEMHYD3D [35], etc.

## 382 **6 Solved problems**

383 Development of the SIFEL package was motivated by real civil engineering problems that  
384 were solved at our department. The software was used for a variety of problems starting  
385 with dynamics of bridges, rock slope stability, analysis of tunnel sheeting, foundation  
386 slabs and finishing with complex coupled problems such as analysis of a nuclear power  
387 plant containment.

388 A complex analysis of the reactor vessel in the UK was the first coupled problem  
389 solved with METR. The problem was solved within the scope of European project MAE-  
390 CENAS whose topics were connected with prolongation of the service life of nuclear  
391 power plants. The problem was solved as a coupled thermo-hydro-mechanical analysis

392 and more details can be found in [22].

393 The problem of the lift layer separation on bridge decks was another coupled thermo-  
394 hydro-mechanical analysis solved using METR. This problem was observed during re-  
395 construction of bypass road bridge in Valašské Meziříčí (Czech Republic). The recon-  
396 structed lift layer was relatively thin (10~12 cm) and it caused large crack propagation  
397 due to shrinkage. In addition, the important role of climate conditions during casting  
398 was acknowledged. Proper curing procedure and reinforcement were proposed on the  
399 basis of the performed analyses which are described in paper [16].

400 The most complex coupled problems solved by METR are presented in the follow-  
401 ing subsections. High demands of these problems were caused by complex geometry,  
402 the amount of modelled details, complexity of material models and the high number of  
403 performed time steps.

## 404 6.1 Watertightness of foundation slabs

405 High performance concrete in the diaphragm walls and foundation slabs was one of the  
406 topics of the CIDEAS project in whose scope, the research of watertightness of foundation  
407 slabs was carried out. The motivation of this research was the construction of a commer-  
408 cial building in Prague (Czech Republic) near the Vltava river. The building was founded  
409 on a slab 10 meters under the ground-water level which led to the increased demands on  
410 watertightness of the used concrete.

411 Foundation slabs are often built in deep ditches under the ground-water level and  
412 they can have a significant thickness. The watertightness is influenced by a variety of  
413 factors, especially:

- 414 • concrete mixture composition,
- 415 • degree and form of reinforcement,
- 416 • technology of casting procedure,
- 417 • arrangement of working gaps,
- 418 • proper curing of concrete during hydration.

419 Watertight concrete is often designed as high-performance, self-compacting or easy-  
420 compacting where, except the basic material parameters such as water-cement ratio and  
421 particular aggregates, an important role also play the admixtures such as superplasti-  
422 fiers and accelerators. These admixtures influence significantly evolution of hydration  
423 heat and autogeneous shrinkage whose values are raised when compared to the usual  
424 concrete.

425 These factors are necessary to take into account in computer simulation of slab be-  
426 haviour. The computer simulation should represent

- 427 • used casting procedure by particular layers and shrinkage parts (the slab has to be  
428 cast in several layers with thickness 400~600 mm),
- 429 • curing of concrete (watering and protection against sun radiation),

- 430 • autogeneous shrinkage in early stages,
- 431 • drying shrinkage in late stages,
- 432 • increasing stiffness and strength of concrete in course of time,
- 433 • creep of concrete,
- 434 • possible damage of concrete.

435 All these effects depend on time, temperature and humidity and thus the coupled thermo-  
436 hydro-mechanical analysis should be performed.

437 The foundation slab of the mentioned commercial building in Prague was analyzed  
438 by a staggered approach where the transport processes influenced the mechanical analy-  
439 sis. It should be emphasized that the heat and moisture transfer were fully coupled.

440 The slab is created from two parts which are mutually shifted 1.3 m. The thickness of  
441 slab is 1 m and the spans are 15.0 and 15.8 m. On the boundaries are left shrinkage bands  
442 whose width is 1.5 m. The scheme of the slab is depicted in Fig. 1.

443 The slab was reinforced by 12 bars of reinforcement V25 per meter in longitudinal and  
444 transversal directions. There were also ties made from reinforcement V16 whose density  
445 was 9 pieces per square meter.

446 The slab was cast in three layers of the thickness of approximately 33 cm in order to  
447 avoid the damage due to the generated hydration heat. The cast sections were watered  
448 for three days and they were covered by PE sheets after casting. The generation of hydra-  
449 tion heat during first several hours and damage evolution due to shrinkage and thermal  
450 strains were the reasons for small time steps used at the beginning of analysis. Damage  
451 evolution causes the increase of the norm of the unbalanced force vector in the Newton-  
452 Raphson method and if the time step is not chosen carefully, convergence problems arise.

453 The computer simulation begins at 1 hour after the end of casting of the first layer. In  
454 the performed thermo-hydro-mechanical analysis, the Künzel-Kießl's model was used  
455 for modelling of transport processes, the B3 creep model and the scalar isotropic damage  
456 model were used for the description of the mechanical behaviour. These models were  
457 in SIFEL computer code complemented by a hydration heat model for concrete and by  
458 statistically processed data of climatic conditions for Prague region. The slab was sup-  
459 ported by springs at the bottom. Stiffness of the springs near the corners were increased  
460 in order to capture of subsoil behaviour. A dead weight load was applied on the whole  
461 slab. An important role was played by the thermal boundary conditions used in the heat  
462 transfer analysis. In this case, thermal boundary conditions simulated the average aerial  
463 daily temperatures in June and they were obtained by long-term measurements in the  
464 given region.

465 Thermo-hydro-mechanical coupled problems have very large demands on computa-  
466 tional power. Because many material models were coupled together, an extraordinarily  
467 large number of internal variables were stored in each integration points. The stored  
468 internal variables and the large matrix of the system of algebraic equations led to ex-  
469 tremely large demands on computer memory. In this case, the memory space used for  
470 internal variables and memory space used for the system matrix are comparable. Taking

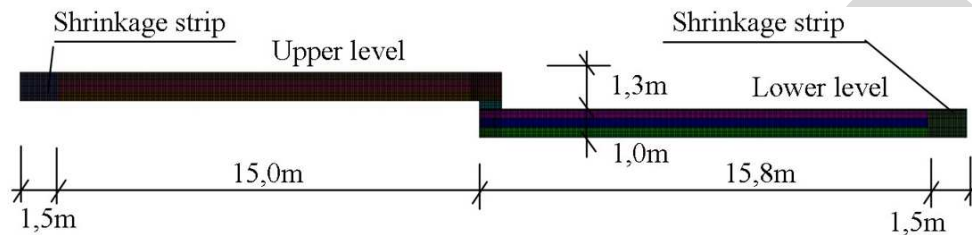


Figure 1: Dimensions of the model and finite element mesh – section view.

471 into account the memory requirements, the 2D model of the problem was created even  
 472 though the program can solve 3D problems as well as the material models are derived  
 473 for 3D too. The use of 2D elements reduces the number of both internal variables and  
 474 unknowns. The reduced number of unknowns is also important for the speed of factor-  
 475 ization of the equation system (4.5). The factorization has to be performed once or several  
 476 times at each time step depending on the results from the Newton-Raphson method that  
 477 has to be used due to non-linearities hidden in the scalar isotropic damage model.

478 The sizes of finite elements used were about 4 cm in both directions except of the thin  
 479 bottom and top layers where the mesh is twice finer in the transversal direction. The  
 480 necessity of the finer mesh is given by increased temperature and humidity gradients in  
 481 these layers and the consequent damage occurrence. Details of mesh decomposition are  
 482 captured in Fig. 2.

483 The generated mesh takes into account the sequential casting procedure and the par-  
 484 ticular concrete layers are generated with different material properties. In Figs. 1 and 2,  
 485 these layers are drawn by various colours.

B3 model was used for the creep and shrinkage description, which involves evolution  
 of Young's modulus with respect to age of concrete while the scalar isotropic damage  
 model assumed the material parameters to be constant. It was especially necessary to  
 introduce a time dependent evolution of the tensile strength. In this case, a simple linear  
 function was assumed

$$f_t(t) = cE(t), \quad (6.1)$$

486 where  $c$  is material parameter and  $E(t)$  is the value of time dependent Young's modulus  
 487 which was calculated by the B3 model. The material parameters for concrete class C35/45  
 488 were used in the B3 model and  $c$  was set to  $10^{-4}$ .

489 Two conclusions follow from the results of the coupled heat and moisture transfer  
 490 analysis and from the simultaneous mechanical analysis. The first is that the accumu-  
 491 lated hydration heat expires approximately after 7 days (Fig. 3) simultaneously with au-  
 492 togenous shrinkage phase. The second conclusion is that during the process of drying,  
 493 the drop of moisture content and temperature occurs first in the surface layers and much  
 494 later in the core. The effect of the diffusion process of drying (shrinkage of concrete) on  
 495 the stress development and micro-cracks distribution is rather extensive. Smearred cracks  
 496 can cause the initialization of main cracks.

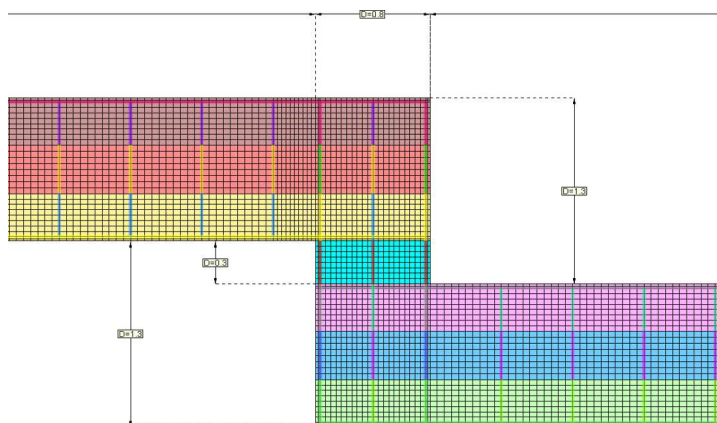


Figure 2: Detail of FE mesh near drop.

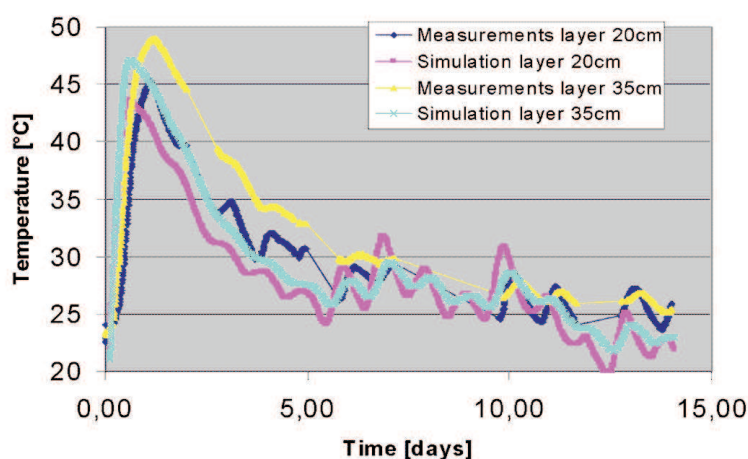


Figure 3: Temperature history.

497 The following figures depict the resulting course of the normal stresses  $\sigma_x$  (Fig. 4), the  
 498 shear stresses  $\tau_{xy}$  (Fig. 5), the deformed shape of the structure (Figs. 6-8) and the damage  
 499 parameter  $\omega$  (Figs. 9-11) for particular construction stages of the lower slab. The results  
 500 were calculated at the time shortly before the casting of the next layer for the two bottom  
 501 layers and for the top layer, they were calculated at the time of 15 hours since casting of  
 502 the first layer. Detailed views of the damaged areas are captured in Figs. 12 and 13.

503 The results of the analysis confirmed that the correct modelling of the sequential con-  
 504 struction influences the evolution of the damage parameter significantly. In Fig. 12, the  
 505 distribution of nonzero values of the damage parameter can be seen on the bottom layer  
 506 which extends to 20 cm of its thickness. The maximum value of the damage parameter is  
 507 0.4. The damage is caused by hydration heat generation of the top layer which is delayed  
 508 when compared to the bottom layers. The peak of hydration heat generation in the top



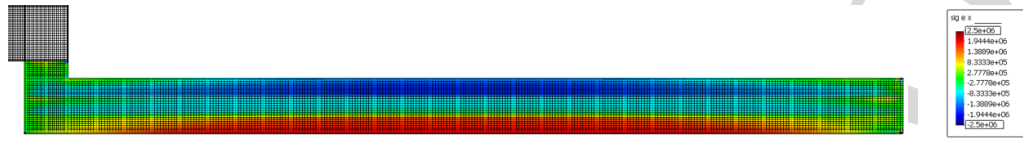


Figure 4: Distribution of stresses  $\sigma_x$ .

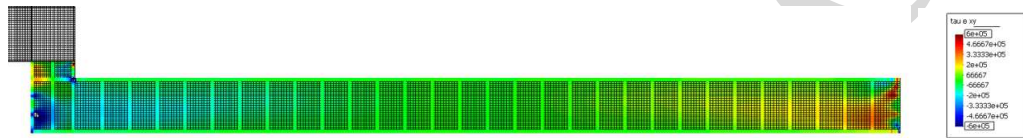


Figure 5: Distribution of stresses  $\tau_{xy}$ .

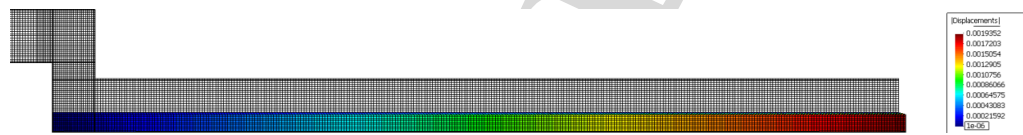


Figure 6: Deformed shape of the first layer of concrete.

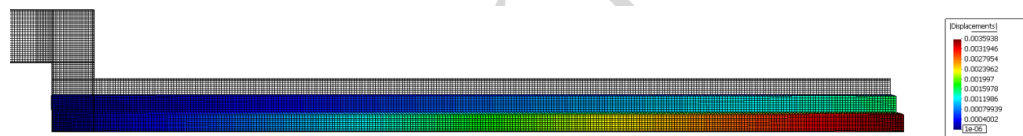


Figure 7: Deformed shape of the second layer of concrete.

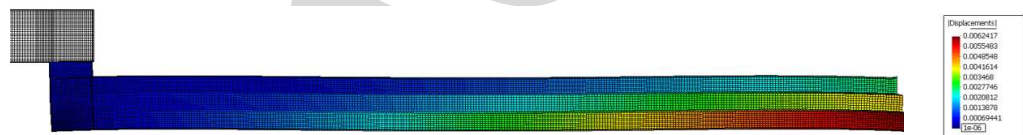


Figure 8: Deformed shape of the third layer of concrete.

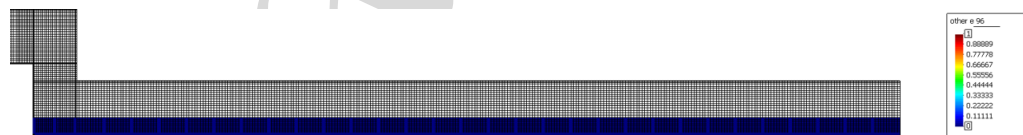


Figure 9: Distribution of the damage parameter  $\omega$  in the first layer of concrete.

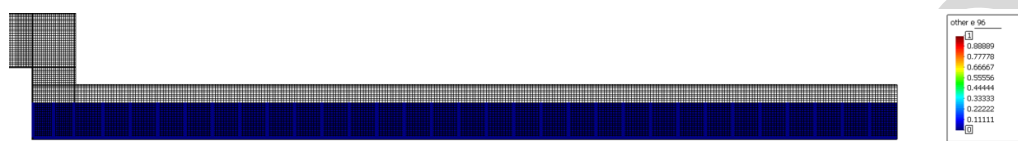


Figure 10: Distribution of the damage parameter  $\omega$  in the second layer of concrete.

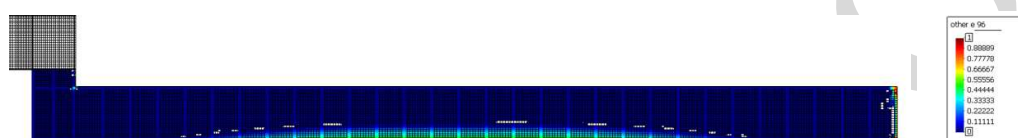


Figure 11: Distribution of the damage parameter  $\omega$  in the third layer of concrete.

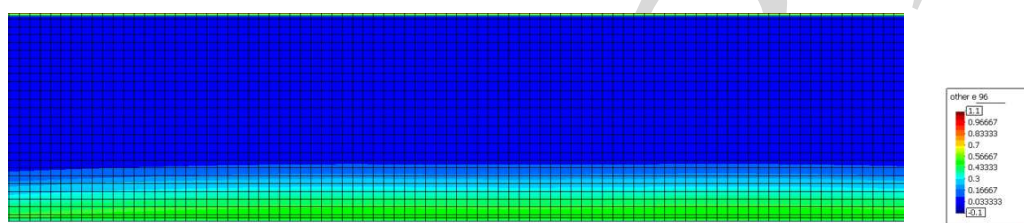


Figure 12: Distribution of the damage parameter  $\omega$  in the middle of the slab.

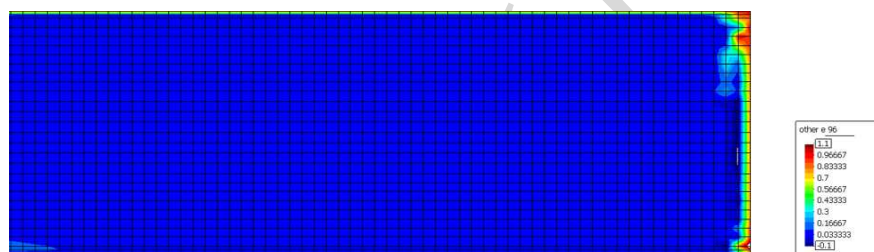


Figure 13: Distribution of the damage parameter  $\omega$  in the right corner of the slab.

509 layer causes nonuniform distribution of thermal strains and consequently, the slab tends  
 510 to deflect upward. In the middle of the slab, the influence of dead weight load domi-  
 511 nates and it leads to the damage of the bottom layer. The resulting deformed shape of the  
 512 structure is captured in Fig. 8.

513 Another factor causing damage are the climate conditions. It can be observed in  
 514 Fig. 12 that the whole top surface is damaged but only to a shallow depth. The damage  
 515 was caused by drying shrinkage which was intensified by the applied climatic condi-  
 516 tions. The last area with significant damage evolution is at the top right corner of the slab  
 517 (see Fig. 13). In this case, the damage was caused by shear stresses whose concentration  
 518 at the corner can be observed in Fig. 5.

## 519 **6.2 Computer simulation of reactor vessel**

520 Reliability and durability of reactor containments depend directly on the prestressing  
521 system. General results from in-situ measurements during the whole time of operation  
522 show the increase of deformations and the increase of prestress losses since the onset of  
523 service. Most measurements also indicate that the temperature has a major influence on  
524 the prestress losses. These conclusions were obtained, e.g., from thirty years of measured  
525 prestress at Swedish nuclear reactor containments [1]. This section presents a computer  
526 simulation of a nuclear power plant containment under cyclic temperature loading dur-  
527 ing service, when stages of service and planned stops are changed. It is well known that  
528 the increase of temperature influences the rate of concrete creep. This fact can cause sig-  
529 nificant prestress losses of the structure. Moreover, increasing deformations are observed  
530 and additional cracks could occur. An advanced two-level model is used for predicting  
531 the prestress losses and the structure response. It is a combination of a global macro-  
532 level model and a local model. The aim of the global one is the modelling of evolution  
533 of prestress forces changed by the temperature and climatic loading. The local model  
534 is loaded by the mechanical and thermal loading from the global model. The staggered  
535 coupled thermo-mechanical analysis is the main part of the local model which has to ex-  
536 plain the time dependent processes in the containment wall. The heat transfer analysis  
537 is running in parallel with the mechanical analysis where the temperature effect on con-  
538 crete creep is modeled by Bazant's microprestressing-solidification theory. The local model  
539 is subsequently completed by suitable damage models.

540 The presented study is a part of the global reliability and durability model of nuclear  
541 power plant containment in Temelín in the Czech Republic. The presented computation  
542 attempts to model and explain the increase of radial deformation and decreasing of ten-  
543 don forces since the onset of service. There was a lot of measurements to explain this  
544 phenomena at Swedish nuclear reactor containment with non-injected (non-bounded)  
545 prestress tendons [1] in the time period of 5 years (6.5 years in Czech Republic). Time  
546 evolution of the tendon force is plotted in logarithmic scale in Fig. 14.

547 Two gradients of the tendon force losses were also observed in prestress measure-  
548 ments at the Czech containment. With reference to [1] and discussions in theoretical  
549 studies [5] and [11], it can be concluded that the increase of temperature influences ac-  
550 celeration of creep. Every change of temperature, moisture content, and loading causes  
551 changes of creep rate [5]. There is no doubt that the temperature is one of the sources  
552 of prestress losses increase. The influence of temperature will be the dominant phe-  
553 nomenon, the damage will have the minor effect, and the radial strains increase will  
554 be neglected.

### 555 **6.2.1 Basic data**

556 The containment of the nuclear power plant in the Czech Republic is a monolithic post-  
557 tensioned structure made from reinforced concrete. It consists of two parts – the lower  
558 cylindrical part and the upper dome. The cylinder has the internal diameter of 45.00 m

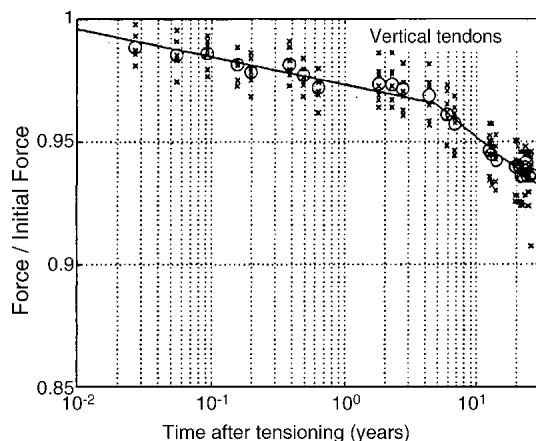


Figure 14: Change of tendon force gradient since service time [1].

559 and the wall is 1.20 m thick. The dome is fixed into a massive girder. The scheme of the  
 560 structure is in Fig. 15. The leak-proofness of the containment is secured by the 8 mm thick  
 561 steel lining placed inside the structure. Unbonded tendons are placed in three parallel  
 562 layers in the containment wall.

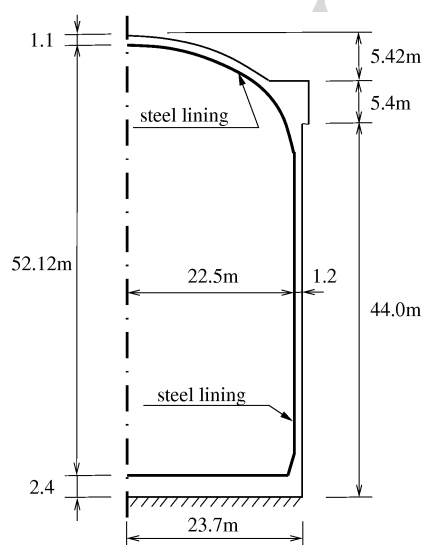


Figure 15: Geometry – section view of the containment.

### 563 6.2.2 Local model

564 **Geometry.** The local model – the cylindrical segment represents a periodic unit cell  
 565 (PUC) from the cylindrical part of the containment with channels for prestressing ten-  
 566 dons and with vertical, radial and horizontal reinforcement. It is captured in Fig. 17.

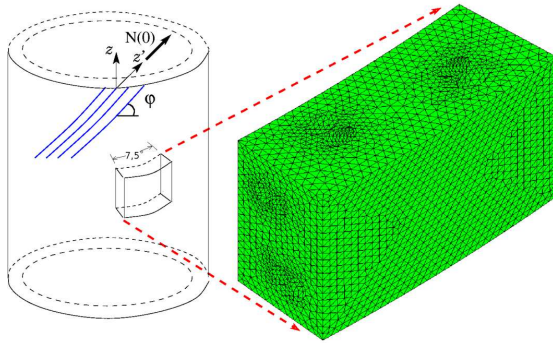


Figure 16: Scheme of PUC.

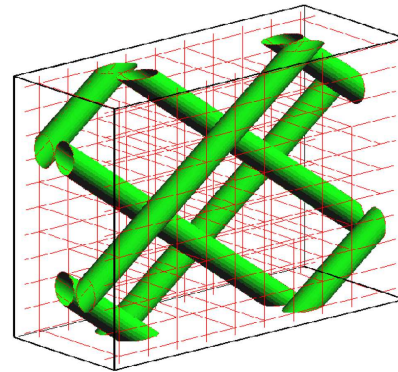


Figure 17: Tendon channels and reinforcement.

567 The height of PUC is 2.12 m and it covers the section of the angle of  $7.5^\circ$  (Fig. 16). The  
 568 prestressing tendons are not modeled. Their effect is introduced as mechanical loading.

569 The finite element mesh was generated by the automatic mesh generator T3D [39].  
 570 The thermo-mechanical coupled algorithm of the finite element computer code SIFEL  
 571 [32] was used.

### 572 6.2.3 Loading

573 **Temperature loading.** The impact of temperature is modeled by the Dirichlet boundary  
 574 conditions. Temperatures from in-situ measurements (inner and outer surface) are ap-  
 575 plied directly into computation. The temperature cycle loading depicted in Fig. 18 was  
 576 considered in one year intervals.

577 **Mechanical loading.** Mechanical loading of the cylindrical segment is considered as a  
 578 combination of four types of loading: (i) Dead weight of the segment. (ii) Dead weight

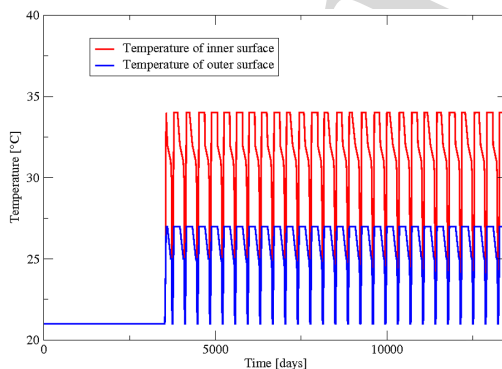


Figure 18: Temperatures of inner and outer surface considered in the computer simulation since the end of construction.

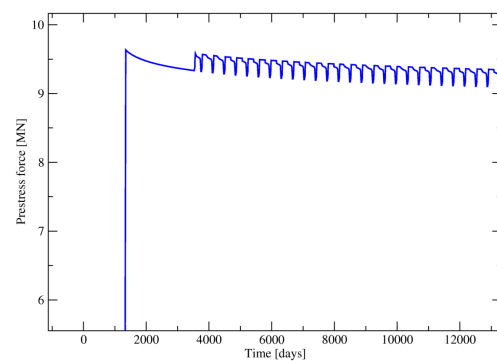


Figure 19: Change of the prestress force in the anchorage system since the end of construction.

579 of the containment over the segment is considered as a loading on the top surface. (iii)  
580 Vertical loading of the prestress forces is considered also as loading on the top surface.  
581 It is computed from the reactions of the anchorage system decreased by prestress losses  
582 caused by friction in tendon channels. (iv) Loading prescribed directly in tendon chan-  
583 nels is consisting of radial and tangential components.

584 The first two loadings are instantaneous. The latter two loadings are calculated as  
585 a multiple of prestress forces in tendons in place of the anchorage system. The values  
586 of prestress forces are obtained from in-situ measurements by a magneto-elastic method  
587 (MEM) and they are displayed in Fig. 19. The data were approximated by a logarithmic  
588 regression method. In the graph, jumps which simulate in the cycle service time – the  
589 planned stop are obtained from the global model.

590 **Material properties and equations.** In the transport part of the problem, the non-  
591 stationary heat transport was solved assuming constant material parameters. The me-  
592 chanical part of the computation considered four types of constitutive material models,  
593 namely creep, damage, plasticity and the thermal dilatation. The B3 creep model influ-  
594 enced by temperature and moisture changes and a damage model describe the behaviour  
595 of concrete. Several damage models were used in the computer simulation. There were  
596 local and non-local versions of scalar isotropic damage model, anisotropic damage model  
597 and orthotropic model. Results obtained using the orthotropic model showed the best co-  
598 incidence with in-situ measurements. The application of damage models is described in  
599 detail in [17]. The steel reinforcement was modeled using the bar finite elements with  
600 plasticity model using Huber-Mises-Hencky condition. The thermal dilatation model  
601 was assumed in both materials (concrete and reinforcement).

#### 602 6.2.4 Results of computation and conclusions

603 The relation between the response of the local model and the tensile strength of concrete  
604 in damage models was observed during the computer simulation. Hence, there were  
605 made several calculations with different tensile strengths in order to verify the damage  
606 evolution. The scalar isotropic damage model gives the upper estimate because the dam-  
607 age parameter influenced all principal directions.

608 Therefore, the more realistic anisotropic or orthotropic models should be used in a  
609 reliable prognosis of the containment durability. The distribution of damage parameter  
610 for orthotropic damage model is captured in Fig. 20.

611 From the concrete creep point of view, the different levels of the temperature effect on  
612 concrete creep were also studied. In term of explanation of the increase of radial defor-  
613 mation, the most monitored graphs are strains in radial reinforcement depicted in Fig. 21.  
614 It can be concluded from the data of the analysis that the temperature effect, which in-  
615 creases concrete creep, is vanishing in time. In the case of some accompanying effect due  
616 to cracking strain evolution, the increase of radial deformation and decreasing of tendon  
617 forces during service life can be observed. The strains in the radial reinforcement are  
618 plotted in Fig. 21 in comparison with the average data from in-situ measurements.



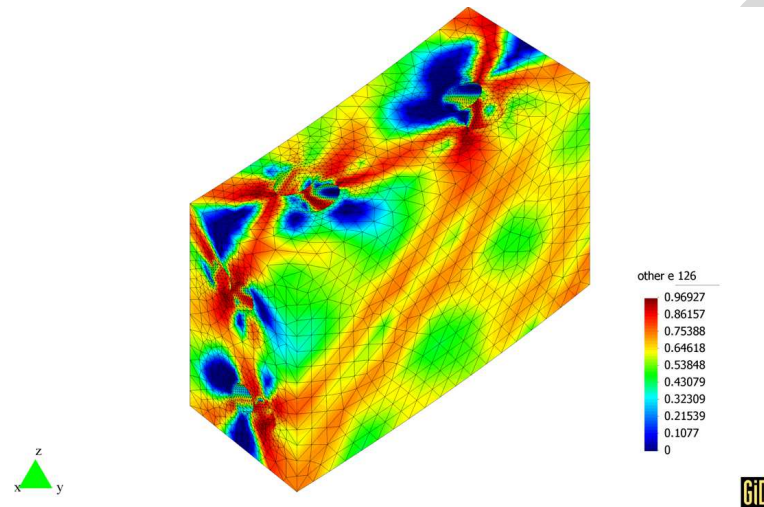


Figure 20: Isosurfaces of damage parameter in time of 6000 hours since the end of construction.

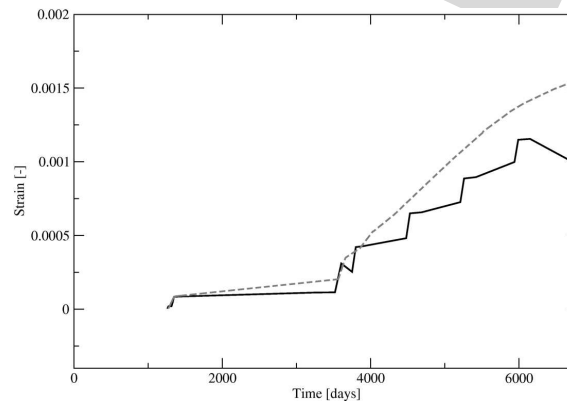


Figure 21: Comparison of strain in radial reinforcement obtained from computation (solid line) and from in-situ measurements (dashed line – averaged data).

619 Conclusions from the results of analysis are the following:

- 620 • The explanation of the increase of radial strains and decreasing of tendon forces
- 621 since the onset of service is based on the theoretical knowledge in concrete creep
- 622 influenced by the temperature changes and partly on the prestress losses measure-
- 623 ments mainly at Swedish nuclear reactor containments. The influence of the temper-
- 624 ature increase during the service was proved.
- 625 • The results obtained from the connection of the simplified global model and the
- 626 local model show relatively good coincidence with in-situ measurements.
- 627 • For the best coincidence between the computer simulation and the measurements,
- 628 calibration of all appearing material models and their parameters should be per-

629 formed and compared with laboratory and in-situ measurements. Especially, the  
630 tensile strength which is the basic property for monitoring the hypothetical dam-  
631 age of the containment has to be determined.

## 632 7 Conclusions

633 The coupled hydro-thermo-mechanical analysis was successfully used for description of  
634 behaviour of several complicated concrete structures. Creep and damage models were  
635 coupled with heat and moisture effects which enabled description of structure response  
636 from construction till the end of service life. In several cases, parallel computers were  
637 used because of the extremely large demands on computer memory and power. Future  
638 development will be devoted to multiscale modelling which can lead to better results,  
639 especially in the early stages of concrete. The application of hp-version of the finite ele-  
640 ment adaptivity is promising because it reduces the number of unknowns and therefore  
641 the computer memory.

## 642 Acknowledgments

643 Financial support for this work was provided by the Czech Science Foundation, projects  
644 n. 103/08/1119 and 105/10/1682. Another financial support was provided by the Min-  
645 istry of Education, Youth and Sports of the Czech Republic, project No. 1M0579. The  
646 financial support is gratefully acknowledged.

## 647 References

- 648 [1] P. Anderson, Thirty years of measured prestress of Swedish nuclear reactor containment,  
649 Nucl. Eng. Des, 235 (2005), 2323-2336.
- 650 [2] Z. P. Bazant, Mathematical Modeling of Creep and Shrinkage of Concrete, John Wiley&Sons,  
651 Chichester-Singapore, 1988.
- 652 [3] Z. P. Bazant and S. Baweja, Creep and Shrinkage Prediction Model for Analysis and Design  
653 of Concrete Structures – Model B3, Mater. Struc, 28 (1995) 357-365.
- 654 [4] Z. P. Bazant and Chern (1985a) Concrete creep at variable humidity: constitutive law and  
655 mechanism. Mater. Struc, (RILEM, Paris), 18, Jan., 1-20.
- 656 [5] Z. P. Bazant, G. Cusatis and L. Cedolin, Temperature effect on concrete creep modeled by  
657 microprestress-solidification theory, J. Eng. Mech-ASCE, Vol. 130, N. 6 (2004), 691-699.
- 658 [6] Z. P. Bazant, L. J. Najjar (1972) Nonlinear water diffusion in nonsaturated concrete structural  
659 analysis program. Matériaux et constructions, RILEM, Paris, 5(25), 8-9.
- 660 [7] Z. Bittnar and J. Šejnoha, Numerical Methods in Structural Mechanics, ASCE Press, New  
661 York, USA, 1996.
- 662 [8] M. A. Crisfield, Non-linear Finite Element Analysis of Solids and Structures, John Wiley &  
663 Sons Ltd, Chichester, UK, 1991.
- 664 [9] C. Farhat and F. X. Roux, Implicit parallel processing in structural mechanics, Comput.  
665 Mech. Adv., 2 (1994), 1-124.



- 666 [10] D. Gawin, C. E. Majorana, B. A. Schrefler (1999) Numerical analysis of hygro-thermic be-  
667 haviour and damage of concrete at high temperature. *Mech. Cohes-Frict. Mat*, 4, 37-74.
- 668 [11] C. Hellmich, Shotcrete as Part of the New Austrian Tunneling Method: From Thermochemo-  
669 mechanical Material Modeling to Structural Analysis and Safety Assessment of Tunnels, Be-  
670 gutachter: H.A. Mang, F-J Ulm; Institute for Strength of Materials, Vienna University of  
671 Technology, Vienna, Austria, 1999.
- 672 [12] T. J. R. Hughes, The Finite Element Method. Linear Static and Dynamic Finite Element Anal-  
673 ysis, Prentice-Hall, inc. Englewood Cliffs, New Jersey, 1987.
- 674 [13] M. Jirásek and Z. P. Bazant, Inelastic Analysis of Structures, John Wiley&Sons, Ltd, Chich-  
675 ester, UK, 2002.
- 676 [14] K. Kiessl, Kapillarer und dampfförmiger Feuchtetransport in mehrschichtigen Bauteilen.  
677 PhD Thesis, University of Essen, Essen (1983).
- 678 [15] J. Kočí, V. Kočí, J. Maděra, P. Rovnaníková and R. Černý, Computational analysis of hy-  
679 grothermal performance of renovation renders, *Advanced Computational Methods and Ex-  
680 periments in Heat Transfer*, XI (2010), 267-277.
- 681 [16] T. Koudelka and T. Krejčí, An Anisotropic Damage Model for Concrete in Coupled Prob-  
682 lems, *Proceedings of the Ninth International Conference on Computational Structures Tech-  
683 nology*, B. H. V. Topping and M. Papadrakakis, Civil-Comp Press, Stirlingshire, UK, 2008,  
684 paper 157.
- 685 [17] T. Koudelka, T. Krejčí and J. Šejnoha, Analysis of a Nuclear Power Plant Containment, *Pro-  
686 ceedings of the Twelfth International Conference on Civil, Structural and Environmental  
687 Engineering Computing*, B. H. V. Topping, L. F. Costa Neves and R. C. Barros, Civil-Comp  
688 Press, Stirlingshire, UK, 2009, paper 132.
- 689 [18] T. Krejčí, T. Koudelka, J. Šejnoha and J. Zeman, Computer Simulation of Concrete Structures  
690 subject to Cyclic Temperature Loading, *Proceedings of the Twelfth International Conference  
691 on Civil, Structural and Environmental Engineering Computing*, B. H. V. Topping, L. F. Costa  
692 Neves and R. C. Barros, Civil-Comp Press, Stirlingshire, UK, 2009, paper 131.
- 693 [19] J. Kruis, Domain Decomposition Methods on Parallel Computers, *Progress in Engineering  
694 Computational Technology*, B. H. V. Topping and Mota Soares, C. A., Saxe-Coburg Publica-  
695 tions, Stirling, Scotland, UK, (2004), 299-322.
- 696 [20] J. Kruis, Domain Decomposition Methods for Distributed Computing, Saxe-Coburg Publi-  
697 cations, Kippen, Stirling, Scotland, UK, 2006.
- 698 [21] J. Kruis, The FETI Method and its Applications: A Review, *Parallel, Distributed and Grid  
699 Computing for Engineering*, B. H. V. Topping, and P. Iványi, Saxe-Coburg Publications, UK,  
700 (2009), 199-216.
- 701 [22] J. Kruis, T. Koudelka and T. Krejčí, Efficient computer implementation of coupled hydro-  
702 thermo-mechanical analysis, *Math. Comput. Simulat*, 80 (2010), 1578-1588.
- 703 [23] H. M. Künzel and K. Kiessl, Calculation of heat and moisture transfer in exposed building  
704 components, *Int. J. Heat Mass Tran*, 40 (1997), 159-167.
- 705 [24] J. Lemaitre and J. L. Chaboche, *Mechanics of solid materials*, Cambridge University Press,  
706 Cambridge, UK, 1994.
- 707 [25] J. Maděra, J. Kočí, V. Kočí, J. Výborný and R. Černý, Computational prediction of hy-  
708 grothermal conditions in innovated AAC-based building envelopes, *Advanced Computa-  
709 tional Methods and Experiments in Heat Transfer*, XI (2010), 291-301.
- 710 [26] C. Majorana, J. Mazars, Thermohygro-metric and mechanical behaviour of concrete using  
711 damage models, *Materials and Structures*, 30 (1997), 349-354.
- 712 [27] J. Mazars and G. Pijaudier-Cabot, Continuum damage theory – application to concrete, J.

- 713 Eng. Mech-ASCE, 115 (1989), 345-365.
- 714 [28] E. Papa and A. Taliercio, Anisotropic Damage Model for the Multiaxial Static and Fatigue  
715 Behaviour of Plain Concrete, Eng. Fract. Mech, Vol. 55, No. 2 (1996), 163-179.
- 716 [29] C. R. Pedersen, Combined heat and moisture transfer in exposed building constructions.  
717 PhD Thesis, Technical University of Denmark, Lingby (1990).
- 718 [30] S. Pietruszczak and Z. Mróz, Finite element analysis of deformation of strain-softening ma-  
719 terials, Int. J. Numer. Meth. Eng, 17 (1981), 327-334.
- 720 [31] A. Quarteroni and A. Valli, Domain Decomposition Methods for Partial Differential Equa-  
721 tions, Oxford University Press Inc., New York, USA, 1999.
- 722 [32] SIFEL – Simple Finite Elements, <http://mech.fsv.cvut.cz/~sifel/index.html>,
- 723 [33] J. Skrzypek and A. Ganczarski, Modeling of Material Damage and Failure of Structures,  
724 Springer-Verlag Berlin Heidelberg, Germany, 1999.
- 725 [34] B. Smith, P. Bjørstad and W. Gropp, Domain Decomposition. Parallel Multilevel Methods for  
726 Elliptic Partial Differential Equations, Cambridge University Press, Cambridge, UK, 1996.
- 727 [35] V. Šmilauer and T. Krejčí, Multiscale Model for Temperature Distribution in Hydrating Con-  
728 crete, International Journal for Multiscale Computational Engineering, Vol. 7, N. 2 (2009),  
729 135-151.
- 730 [36] P. Šolín, J. Červený and I. Doležel, Arbitrary-level hanging nodes and automatic adaptivity  
731 in the hp-FEM, Math. Comput. Simulat, Vol. 77, Iss. 1 (2008), 117-132.
- 732 [37] P. Šolín, L. Dubcová and J. Kruis, Adaptive hp-FEM with dynamical meshes for transient  
733 heat and moisture transfer problems, J. Comput. Appl. Math, Vol. 233, Iss. 12 (2010), 3103-  
734 3112.
- 735 [38] P. Štemberk and P. Kalafutová, Modeling very early age concrete under uniaxial short-time  
736 and sustained loading, Mechanika, Vol. 70, N. 2 (2008), 16-21.
- 737 [39] T3D – automatic mesh generator, <http://mech.fsv.cvut.cz/~dr/t3d.html>,
- 738 [40] A. Toselli, and O. Widlund, Domain Decomposition Methods – Algorithms and Theory,  
739 Springer-Verlag, Berlin, Germany, 2005.